The APOE-R136S mutation protects against APOE4-driven Tau pathology, neurodegeneration, and neuroinflammation

by

Maxine Nelson

DISSERTATION

Submitted in partial satisfaction of the requirements for degree of

DOCTOR OF PHILOSOPHY

in

Biomedical Sciences

in the

GRADUATE DIVISION

of the

UNIVERSITY OF CALIFORNIA, SAN FRANCISCO

Approved:

DocuSigned by:
Erik Ullian
1ACF3D77A55F4F0...

Erik Ullian

Chair

DocuSigned by:
Yadong Huang
DocuSigned by:

Yadong Huang

Sheng Ding
8CDD680BE3E24BD...

Sheng Ding

Committee Members

This work is dedicated to my grandmother, Reine Koretz, and my parents, Kent and Sharon Nelson.

ACKNOWLEDGEMENTS

This thesis was the result of much effort, support, and inspiration from numerous co-workers, family, and friends.

First, I would like to thank my mentor Dr. Yadong Huang, without whom this work would not be possible. Yadong is first and foremost a dedicated scientist, and he guided me to follow the biology as this story revealed itself. He is a supportive mentor who spent many hours discussing my studies and carefully reading my fellowship applications and manuscript drafts. Yadong ensured I had many opportunities to learn both rigorous scientific practices and also how to productively run collaborative studies. I am grateful to have conducted my graduate work in his lab and will take all that I have learned during my graduate training forward throughout my career.

Second, I thank the entire Huang lab. Older students who mentored me when I first began, Ramsey Najm and Emily Jones, provided instrumental guidance and advice about how to succeed in graduate school. I joined the lab along with fellow first-years Nicole Koutsodendris and Antara Rao; I cannot express the extent to which their comradery and friendship lifted me up when I hit experimental roadblocks. We found ourselves in countless APOE rabbit holes when surviving quals and writing our review. The younger graduate student mentees, Jessica Blumenfeld, Oscar Yip, Min Joo Kim, and Zherui Liang, brought positive energy, themed dress-up days, and an inquisitive spirit to the latter half of my thesis work – arguably when a tired graduate student needs this most! Our postdocs Jason Bant and Brian Grone also offered consistent and genuine words of encouragement during long data dry spells that inspired me to persist. Lastly, Seo Yeon Yoon has been a tremendous help with mouse tissue collection and maintaining the mouse lines.

Third, I thank our Gladstone collabotors. First, Dr. Bob Mahley for his advice, encouragement, and scientific feedback on this work. He also helped me attend a conference with a Career Award. The Bioinformatics Core have provided invaluable expertise on all of our transcriptomic analyses and performed all of the snRNAseq work.

Fourth, I thank my thesis committee members, Dr. Erik Ullian, who has been an advocate for my aspirations and offered valuable scientific input, and Dr. Sheng Ding, who has given insightful suggestions and support throughout graduate school.

Fifth, I thank my mentors who inspired me to pursue a doctorate in biomedical sciences: Dr. Chad Barber who introduced me to independent research as my first ever PI and shaped my future research endeavors; Dr. Marcin Apostol who patiently guided me through my first research experiences post-undergrad as my supervisor at ADRx and continues to offer career advice; and Dr. James Treanor who has been an encouraging, thoughtful, and dependable mentor both scientifically and in my career development for the past seven years.

Sixth, I thank my family and friends for unconditional love and support while I prioritized completing my thesis work. My parents, Kent and Sharon Nelson, and family and friends all over the world have continued to cheer me on. They forgive me for an unpredictable schedule taking care of stem cells and never fail to celebrate milestones of my graduate work.

Finally, I would like to thank my partner and boyfriend, Zack Bernholtz. Zack has patiently supported me in completing my thesis work in countless practical and loving ways. From listening to my challenges with assay development to ensuring I always had nutritious food fueling me, he has truly been an absolutely essential source of strength and support.

CONTRIBUTIONS

Chapters I – VI contain text and figures adapted from Koutsodendris, Nelson, Rao, & Huang, published on January 24, 2022 in *Annual Review of Pathology* (PMID: 34460318) and from a manuscript currently under revision.

Yadong and I collaborated on the overall study design and coordinated the experiments. I generated the APOE4-R136S homozygous and heterozygous hiPSC lines, performed the majority of studies, data collections, and analyses, generated all figures, and wrote the manuscript. Peng Liu generated the APOE4-R136S knock-in mice. Ayushi Agrawal, Brian Grone, and Michela Traglia performed the snRNA-seq analyses and assisted on the related figure preparations. Nicole Koutsodendris and Jessica Blumenfeld shared some immunohistochemical protocols and helped on some immunohistochemical studies and data collection. Oscar Yip, Min Joo Kim, and Antara Rao helped on some immunohistochemical studies and data collection. Yanxia Hao isolated cell nuclei and prepared samples for snRNA sequencing. Seo Yeon Yoon managed all mouse lines and helped on mouse brain collection. Qin Xu helped on the experimental design of CRISPR/Cas9-mediated gene editing experiments in hiPSCs and molecular biology in general. Reuben Thomas provided guidance on snRNA-seq analyses. Ayushi Agrawal, Michela Traglia, and Reuben Thomas developed and implemented the two Generalized Linear Mixed Effects Models of the snRNA-seq. Francisco Lopera, Yakeel T. Quiroz, Joseph F. Arboleda-Velasquez, and Eric M. Reiman participated in the original concept development of the study and provided comments on the manuscript. Robert W. Mahley participated in the original concept development of the study, supported the generation of the APOE4-R136S knock-in mice, and provided advice on some experiments and comments on the manuscript. Yadong Huang participated in the original concept development of the study, guided the generation and characterization of APOE4-R136S knock-in mice, provided advice on data analysis and interpretations, edited the manuscript, and supervised the project.

The APOE-R136S mutation protects against APOE4-driven Tau pathology, neurodegeneration, and neuroinflammation

Maxine Nelson

Abstract

Apolipoprotein E4 (APOE4) is the strongest genetic risk factor for late-onset Alzheimer's disease (LOAD), leading to earlier age of clinical onset and exacerbating pathologies. There is a critical need to identify protective targets. Recently, a rare APOE variant, APOE3-R136S (Christchurch), was found to protect against early-onset AD in a PSEN1-E280A carrier. We sought to determine if the R136S mutation also protects against APOE4-driven effects in LOAD. We generated tauopathy mouse and human iPSC-derived neuron models carrying human APOE4 with the homozygous or heterozygous R136S mutation. We found that the homozygous R136S mutation rescued APOE4-driven Tau pathology, neurodegeneration, and neuroinflammation. The heterozygous R136S mutation partially protected against APOE4-driven neurodegeneration and neuroinflammation, but not Tau pathology. Single-nucleus RNA-sequencing revealed that the APOE4-R136S mutation increased disease-protective and diminished disease-associated cell populations in a gene dose-dependent manner. Thus, the APOE-R136S mutation protects against APOE4-driven AD pathologies, providing a target for therapeutic development against AD.

TABLE OF CONTENTS

LIST OF FIGURES

CHAPTER I: INTRODUCTION

1.1 APOE4 and AD

Alzheimer's disease (AD) is the most common dementia, currently affecting an estimated 5.6 million people over the age of 65 in the US alone (10% of this population)[1]. Despite decades of basic and translational research, no cure exists. In fact, there are currently no disease-modifying therapies available, and the pathogenesis of this multifactorial disease remains incompletely understood.

Apolipoprotein E4 (*APOE4*) is the greatest known genetic risk factor for late-onset sporadic Alzheimer's disease (AD)[2–4]. One copy of APOE4 confers greater than three times the risk of developing AD over the more common APOE3 isoform, and the risk increases to over 12-fold with two copies.[5] It exacerbates AD-related pathologies, including amyloid-beta (Aβ) plaques and intraneuronal neurofibrillary tangles (NFTs) composed of hyperphosphorylated Tau (p-Tau)[6–18]. p-Tau spreads throughout the brain interneuronally, and levels of its accumulation and propagation during disease progression correlates with clinical symptoms and neurodegeneration[19]. How APOE4 gives rise to these detrimental effects is not fully known, but several lines of recent evidence connect its toxicity to enhancing Tau pathology. Studies using both mouse and human tissue have implicated APOE-isoform-specific regulation of Tau phosphorylation[7,8,20]. APOE4 has also been linked to higher levels of age-dependent Tau hyperphosphorylation in the hippocampus of mice expressing human APOE4[10], which leads to learning and memory deficits[11,12]. Furthermore, AD patient data of APOE4-dependent differences in brain atrophy is associated with Tau spread[21]. APOE4 has also been shown to increase neurodegeneration and neuroinflammation *in vivo*[6–18].

As APOE4 carriers make up 55–75% of AD cases[22–25], there is a critical need to investigate the roles of APOE4 in AD pathogenesis and to identify protective targets so that its detrimental effects can be mitigated.

1.2 Structure and Function of APOE

APOE is a glycoprotein involved in lipid metabolism and highly expressed in the brain[26]. In brains, APOE is primarily produced in astrocytes but also in neurons and microglia in response to stress or injury[27–33]. It has two functional domains: a receptor-binding region at the amino-terminus and a lipid-binding region at the carboxyl-terminus[3,34,35]. A single residue change between the APOE4(Arg112) and APOE3(Cys112) isoforms alters protein structure and function, including both the amino-terminal receptor-binding region (residues 136–150) and the carboxyl-terminal lipid-binding region (residues 244–275)[4,35–40]. The receptor-binding region is enriched with positively charged amino acids and is responsible for binding with negatively-charged cell surface receptors, including the low density lipoprotein receptor (LDLR), the LDLR-related protein (LRP), and heparin sulfate proteoglycans (HSPGs)[35,40–42]. Mutations within the receptor binding region of APOE can directly alter binding to these receptors. For instance, by substituting a positively-charged arginine residue for the uncharged serine, the affinity of the receptor binding domain for negatively charged HSPGs is diminished[41,43,44]. The C-terminal domain of APOE can also weakly bind with HSPGs, and it can also indirectly modify the function of the N-terminal receptor-binding domain[35]. Therefore, mutations in both regions can directly or indirectly alter the binding of APOE to various cell surface receptors[40–42]. Notably, rare variants of APOE with point mutations near or within these regions, such as APOE2(Cys112, Cys158)[23,45], APOE3-V236E[46,47], and APOE4-R251G[47], are associated with protection against AD.

1.3 Models Used to Study APOE4 in AD (*in vitro* and *in vivo*)

Studying the molecular mechanisms underlying a uniquely human neurodegenerative disease is challenging. Luckily, there are robust *in vitro* and *in vivo* models in the AD field to aid in our understanding of disease pathogenesis.

First, the PS19 mouse is a widely used tauopathy model expressing a transgene encoding for human Tau-P301S[55]. These mice develop robust age-dependent tauopathy and

neurodegeneration. Other labs have crossed the three common human knock-in (KI) APOE (E) variants with PS19 mice (PS19-E2, PS19-E3, PS19-E4)[9]. They found higher p-Tau levels and greater mislocalization from the axon in PS19-APOE4 mice at three months. In older mice, different APOE genotypes resulted in distinct p-Tau staining patterns, with PS19-E4 mice displaying an increase in p-Tau staining patterns associated with greater atrophy. Furthermore, the most insoluble Tau was enriched in brain extract from these mice over PS19-E2 and -E3. Our lab has independently generated loxP-floxed E4-KI and E3-KI mice[56], crossed them with PS19 mice, and found similar pathologies in 10-month-old mice as previously reported[57].

Next, the advancements in human induced pluripotent stem cell (hiPSC) technology and sophisticated gene editing techniques allow scientists to study neurons from AD patients. Key studies have shown that APOE4 specifically causes increased Tau phosphorylation in human neurons. First, hiPSCs derived from an unaffected donor with APOE3 were edited with CRISPR to express APOE4. APOE4-organoids consisting of neurons and astrocytes aged to six months exhibited over twice the levels of p-Tau compared to APOE3-organoids[16]. Next, our group performed neuronal differentiation from iPSCs derived from either AD patients homozygous for APOE4 or healthy donors homozygous for APOE3[8]. APOE4-neurons displayed higher levels of p-Tau. Converting APOE4 cells into APOE3 rescued these phenotypes after neuronal differentiation. This finding was also supported when the phenotype of APOE4-neurons was rescued following treatment with a small molecule structure corrector mimicking APOE3.

1.4 APOE-R136S Mutation and AD

A recent discovery that a rare APOE variant, APOE3-R136S (APOE3-Christchurch)[41], strongly protects against early-onset AD further highlights the importance of studying the rare variants of APOE in AD pathogenesis and protection. The reported patient was protected from the clinical effects of PSEN1-E280A, a highly penetrant mutation causing early-onset AD dementia, for 28 years by the homozygous APOE3-R136S mutation[41]. Further investigation revealed that this

patient displayed extremely high Aβ pathology but minimal Tau burden, hippocampal atrophy, and neuroinflammation[41,48,49]. A major functional effect of the R136S mutation is disruption of its binding to anionic HSPGs[41,43], key cell surface receptors for the lipid transport function of APOE. Intriguingly, HSPGs have been revealed as essential players in the cellular uptake of Tau over the past decade[50–52]. Intraneuronal Tau accumulation and interneuronal Tau propagation during AD progression correlate with neurodegeneration and detrimental clinical effects[19]. Moreover, Tau aggregation and propagation are major targets in the development of disease-modifying therapies for AD[53,54]. The differential contributions of APOE isoforms to Tau pathology, neurodegeneration, and neuroinflammation have been of great interest in recent years, yet the underlying mechanisms remain incompletely understood. The discovery of this AD-protective APOE-R136S mutation raises a fundamental question as to whether the R136S mutation can also protect against APOE4-driven pathologies in late-onset AD.

1.5 Research Purpose

To experimentally and rigorously address this question, we engineered the R136S mutation into the *APOE4* allele background both *in vivo* in human APOE4 knock-in mice[56] and *in vitro* in human induced pluripotent stem cells (hiPSCs) derived from an AD patient with homozygous APOE4[8]. To investigate the effects of the R136S mutation *in vivo* under a disease-relevant condition, we cross-bred the isogenic APOE4 and APOE4-R136S mice with a widely used tauopathy mouse model expressing Tau-P301S (PS19 line)[55]. Using these PS19-APOE mouse and isogenic hiPSC models, in which any changes in pathologies are due solely to the introduction of this mutation overcoming APOE4 effects, we showed that the R136S mutation robustly protects against APOE4-driven AD pathologies and presented potential mechanisms underlying these effects in mice and human neurons.

CHAPTER II: MATERIALS AND METHODS

2.1 Generation of APOE4-R136S Mice on PS19 Background

Generation of APOE4-R136S knock-in mice by CRISPR/Cas-9-mediated gene editing. Human LoxP-floxed APOE-KI (E-KI) mice were previously generated in our lab, in which the entire mouse *Apoe* gene, except exon 1, was replaced by human *APOE3* or *APOE4* gene, respectively[56]. To generate F0 founders of E4-KI mice harboring the R136S mutation (E4-S/S-KI), a CRISPR/Cas9-based knock-in strategy was employed. The guide RNA (gRNA) and single-stranded oligodeoxynucleotide (ssODN) template were paired and injected into fertilized zygotes to introduce the point mutation of R136S into APOE4[58]. gRNAs were designed with multiple online tools, including CCTop[59], CRISPOR[60], and IDT Custom Alt-R® CRISPR-Cas9 guide RNA. To increase editing efficient, gRNAs were selected based on the proximity of their cutting site to the expected mutation, high targeting efficiency, and low predicted off-target effects.

To generate sgRNA, crRNA (GCTTGCGCAGGTGGGAGGCG) was combined with tracrRNA in a 1:1 ratio (Integrated DNA Technologies, Inc. (IDT)), heated to 95°C for 5 min, and allowed to slowly cool to room temperature (RT). Cas9 protein (IDT) was added to form the Cas9-ribonucleoprotein (Cas9-RNP) complex. The ssODN donor repair template was synthesized by IDT

(G*G*AGGACGTGCGCGGCCGCCTGGTGCAGTACCGCGGCGAGGTGCAGGCCATGCTCG
GCCAGAGCACCGAGGAGCTGCGGGTGAGCTTAGCCTCCCACCTGCGCAAGCTGCGTAAG
CGGCTCCTCCGCGATGCCGATGACCTGCAGAAGCGCCTGGCAGTGTACCAGGCCGGGGC
CCGC*G*A) and added later to prepare for injection. The ssODN was designed to convert APOE4 to APOE4-R136S with a silent mutation at the protospacer adjacent motif (PAM) site to prevent repeated Cas9 editing. Two phosphorothioate modifications were required to protect the ends.

To prepare fertilized zygotes, super-ovulated female C57BL/6 mice (4 weeks old) were mated to E4-KI males. Fertilized zygotes (1-cell stage) were collected from oviducts and injected with Cas9 protein (20 ng/ul), crRNA and tracrRNA (15 ng/ul), and ssODN template (10 ng/ul) into pronucleus of the fertilized zygotes. The injected zygotes were implanted into oviducts of

pseudopregnant CD1 female mice. Positive F0 founders were identified by genomic DNA (gDNA) screening. First, for F0 pups, 3–5 mm tail tips were cut and digested by Proteinase K for gDNA extraction at the age of 4 weeks. A 530-bp genomic region of the *APOE* exon-4 covering the targeted mutations, including 112R and 136R/S, was amplified by PCR using primers (FW 5'*TAAGCTT*GGCACGGCTGTCCAAGGA3' and REV 5'GCTGCATGTCTTCCACCAG3') with high fidelity KOD Plus DNA polymerase (F0934K, TOYOBO). This 530-bp PCR product was used as the template of real-time PCR screening with primers designed to include the expected mutation at the 3' end: FW 5'GGAGCTGCGGGTGAGCTTA3' and REV 5'CTGGTACACTGCCAGGCG3'. With these mutation-specific primers, potential positive F0 candidates showed a much smaller ΔCt (<2) when compared to the Ct value of internal control primers. Lastly, the 530-bp PCR product was used to verify the existence of the expected mutation by Sanger DNA sequencing. The *APOE* gene sequence in F1 breeders was verified to be unaltered except for the expected R136S mutation. CRISPOR was used to predict all potential off-target sites in the genome[60], and those sites located in exon regions on chromosome 7 were verified to be intact via Sanger sequencing.

Generation of tauopathy mice expressing E4, E3, or E4-S/S. The E3, E4, and E4-S/S mice were crossbred with PS19 mice expressing human P301S 1N4R Tau driven by the PrP promoter [B6;C3-Tg(Prnp-MAPT*P301S)PS19Vle/J from The Jackson Laboratory] to generate PS19-E4, PS19-E3, PS19-E4-S/S, and PS19-E4-R/S mice. All mice were on a pure C57BL/6 genetic background and were housed in a pathogen-free barrier facility on a 12 hr light cycle at 19–23°C and 30–70% humidity. Animals were identified by ear punch under brief isoflurane anesthesia and genotyped by PCR of a tail clipping as described above. All animals otherwise received no procedures. All animal experiments were conducted in accordance with the guidelines and regulation of the National Institutes of Health, Institutional Animal Care and Use Committee at the University of California, San Francisco, and the Gladstone Institutes under the protocol AN176773.

2.2 Generation of Isogenic APOE-R136S hiPSC Lines and Neuronal Differentiation

hiPSC culture. The E4/4 hiPSC line was generated as described[61,62] from skin fibroblasts of a subject with an APOE4/4 (E4) genotype. The isogenic E3/3 (E3) hiPSC line was generated from this parental E4/4 hiPSC line as previously described[8]. hiPSCs were maintained in mTeSR medium (85850, StemCell Tech) on 6-well plates precoated with hESQ, LDEV-free Matrigel (354277, Corning). The medium was changed daily, and cells were routinely passaged 1:10–1:15 using Accutase (NC9464543, Fishersci) for dissociation. Rho kinase (ROCK) inhibitor (1254, Tocris) was added to medium at 10μM on day of passaging.

Generating and characterizing isogenic E4-S/S and E4-R/S hiPSC lines by CRISPR Cas-9-mediated gene editing. To generate isogenic E4-S/S and E4-R/S hiPSC lines, CRISPR-Cas9 editing strategy was used[63]. sgRNAs were designed using CRISPOR to optimize for distance of cut site to mutation, high targeting efficiency, and minimal predicted off-target sites[58,64]. The top sgRNA was selected after testing cutting efficiency in pooled, nucleofected cells via the Synthego ICE analysis tool (Synthego Performance Analysis, 2019). To further increase on-target efficiency and minimize off-target editing, S.p. HiFi Cas9 Nuclease was used[65].

Once the top sgRNA was selected, the parental E4 hiPSCs were dissociated in Accutase and $8x10^5$ hiPSCs were pelleted prior to resuspension in nucleofection solution (Lonza) per the Amaxa Human Stem Cell Nucleofector Kit 1 (VPH-5012). For Cas9-RNP preparation, 300pmol of sgRNA (CTTACGCAGCTTGCGCAGGT) (Synthego) targeting exon 4 of the *APOE* gene around Arg136 of the APOE4-coding allele and 40pmol of S.p.HiFi Cas9 Nuclease V3 (IDT) were mixed for 10 min at RT. 4μl of Cas9-RNP and 1μl of ssODN donor repair template synthesized by IDT (GGCCTGGTACACTGCCAGGCGCTTCTGCAGGTCATCGGCATCGCGGAGGAGCCGCTTAC GCAGCTTGCGCAGGTGTGAGGCGAGGCTCACCCGCAGCTCCTCGGTGCTCTGGCCGAGC ATGGCCTGCACCTCGCCGCGGTACTGCACCAG) were added to 100μl of cells in nucleofection solution. The ssODN was designed to convert APOE4 to APOE4-R136S with a silent mutation at the PAM site to prevent repeated Cas9 cutting in edited cells. The mixture was transferred to a

cuvette and nucleofected with Nucleofector II (Lonza) at Nucleofector setting A-030. Next, 500µl of prewarmed (37°C) mTeSR medium with 10µM ROCK inhibitor was immediately added into the nucleocuvette to recover nucleofected cells. The cell mixture was then pipetted into a single well of hESQ-Matrigel precoated 6-well plate with mTeSR and 10µM ROCK inhibitor to recover. After 3–5 days, cells were dissociated in Accutase to a single cell solution and plated to obtain individual colonies utilizing both limiting dilution and colony picking methods in mTeSR and CloneR (05888, StemCell Tech) for viability. For limiting dilution, 0.5 cell/well were seeded onto hESQ-Matrigel precoated 48-well plates. For colony picking, $1x10^3$ cells were sparsely plated into an hESQ-Matrigel precoated 10cm dish. After 3–5 days, surviving colonies from both methods were picked, transferred to hESQ-Matrigel precoated 48-well plates, and expanded to isolate gDNA for screening. A genomic fragment spanning the sgRNA target sites on exon 4 of the *APOE* gene was amplified using primers (FW 5'TAAGCTTGGCACGGCTGTCCAAGGA3' and REV 5'GCTGCATGTCTTCCACCAG3') with Qiagen Taq DNA Polymerase using a Quick Start Protocol for GC rich region (Qiagen, 201443). The amplified genomic DNA fragment was Sanger Sequenced. The top predicted off-target cut sites in coding regions by CHOPCHOP[66] and COSMID[67] were verified to be intact by Sanger Sequencing. Each unique hiPSC line was checked for normal karyotype and validated to maintain pluripotency (see Immunocytochemistry and imaging for details). In total, three hiPSC lines homozygous for R136S mutation and two hiPSC lines heterozygous for R136S mutation were generated and fully characterized for use in the current study.

Neuronal differentiation of hiPSCs. hiPSCs were differentiated into neurons as previously described[8,68], with slight modifications to increase yield. Briefly: hiPSCs were dissociated with Accutase for 5–8 minutes before being quenched with warm (37°C) N2B27 medium made of 1:1 DMEM/F12 (11330032, Thermo Fisher) and Neurobasal Media (21103049, Thermo Fisher), 1% N2 Supplement (21103049, Thermo Fisher), 1% B27 (17504044, Thermo Fisher), 1% MEM Non-essential Amino Acids (11140050, Thermo Fisher), 1% Glutamax (35050061, Thermo Fisher),

and 0.5% penicillin–streptomycin (15140122, Thermo Fisher). Dissociated hiPSCs were pelleted by centrifugation, resuspended in embryoid body media [10μM SB431542 (1614, Tocris) and 0.25μM LDN (04-0074, Stemgent) in N2B27] with 10μM ROCK inhibitor (1254, Tocris), and grown in suspension in a T-75 flask (12-565-349, Fisher Scientific). Flasks were shaken manually once per hour for the first 3 hrs of incubation. On day 2, embryoid bodies had formed, and fresh embryoid body medium was replaced (embryoid bodies pelleted, old medium aspirated, cells resuspend in fresh medium) to remove ROCK inhibitor. Embryoid body medium was replaced similarly on days 4 and 6. On day 8, spheres were plated as neural progenitors onto a 10cm dish precoated with growth factor reduced (GFR) Matrigel (CB-40230A, Fisher Scientific). Neural progenitors were allowed to form neuronal rosettes and sustained in N2B27 media alone for days 8–15. Half of the media was replaced every 48–72 hr depending on confluency and media consumption. Neuronal rosettes were lifted on day 16 using STEMdiff™ Neural Rosette Selection Reagent (05832, StemCell Tech) as directed by manufacturer and plated into 3 wells of a 6-well plated precoated with GFR Matrigel in N2B27 with 100ng/ml FGFb (100-18B, Peprotech) and 100ng/ml EGF (AF-100-15, Peptrotech). This N2B27 medium with FGFb and EGF was replaced daily. On day 20, neural progenitors were dissociated with Accutase, quenched with N2B27, and resuspended in STEMdiff™ Neural Progenitor Medium (05833, StemCell Tech) at $1.2x10^6$ cells/2ml for 1 well of 6-well plate, precoated with GFR Matrigel. Neural progenitor cells were fed with fresh Neural Progenitor Medium daily. On day 28, cells were plated as neurons. Neural progenitor cells were dissociated with Accutase, N2B27 media was added to bring volume of cell suspension to 40ml, and cells were filtered through a 40μm cell strainer (08-771-1, Fisher) to ensure single cell suspension. Cells were collected by centrifugation, resuspended in complete neuronal medium (10ng/ml BDNF (450-02, Peprotech) and 10ng/ml GDNF (450-10, Peprotech) in N2B27) with 10nM DAPT (2634, Tocris), counted, and plated at a concentration of $2x10^5$ cells/well onto 12mm coated glass coverslips (354087, Corning) in a 24-well plate. For cells used for immunohistochemical staining, coverslips coated with poly-L-lysine (P4707, Sigma-Aldrich)

and mouse-Laminin (23017015, Gibco) were put into each well prior to cell plating. 75% of culture medium was replaced on maturing neurons every 3–4 days. DAPT was removed after the first week. Most experiments were performed on neuronal cultures that had been differentiated 3–4 weeks. Tau uptake assay experiments were performed on neurons aged 5–6 weeks.

2.3 Immunohistochemical Analysis of PS19-E4-R136S Mice

Collection of mouse tissue. 10-month-old mice were deeply anesthetized with intraperitoneal injections of avertin (Henry Schein) and transcardially perfused for 1 min with 0.9% saline. Right hemi-brains were drop-fixed in 4% paraformaldehyde (15710, Electron Microscopy Sciences), rinsed in PBS (Corning) for 24 hr, and cryoprotected in 30% sucrose (Sigma) for 48 hr at 4°C. The fixed right hemi-brains were sliced into 30µm coronal sections spanning the hippocampus on a freeze sliding microtome (Leica) and stored in cryoprotectant (30% Ethylene Glycol, 30% Glycerol, 40% 1X PBS) at -20°C. Left hemi-brains were snap frozen on dry ice and stored at -80°C for further analyses.

Immunohistochemistry. Several sections from each mouse (30µm thick, 300µm apart) were transferred to a 24-well plate and washed 3x5min with PBS-T (PBS + 0.1% Tween-20) to remove cryoprotectant. For diaminobenzidine (DAB) staining, antigen retrieval was accomplished with citrate buffer (0.1M sodium citrate, 0.1M citric acid in PBS, microwaved until boiling) applied to brain sections for 5 min. Next, sections were washed 2x5min in PBS-T, incubated in endogenous peroxidase block (0.3% H_2O_2 (Sigma) and 10% methanol (Fisher Scientific) in PBS) for 15 min, washed once in PBS-T for 5 min, and blocked for non-specific binding in a solution of 10% Normal Donkey Serum (017000121, Jackson Immuno) and 1% non-fat dry milk in PBS-T for 1 hr at RT. After blocking, sections were washed 2x5min in PBS-T before undergoing an additional avidin/biotin block (SP-2001, Vector Labs) as directed for 15 min and then washed 2x5min in PBS-T. Sections were incubated in M.O.M. blocking buffer (1 drop M.O.M. IgG/4ml PBS-T) (MKB-2213-1, Vector Labs) for 1 hr at RT, washed 2x5min in PBS-T and incubated in primary antibody (AT8 (MN1020, Thermo Fisher Scientific, 1:100)) overnight at 4°C in a solution of 5% normal

donkey serum and PBS-T. The next day, sections were washed in 3x5min with PBS-T and incubated in biotinylated secondary antibody (715-065-150, Jackson Immuno Research, 1:200) for 1 hr at RT. Sections were then washed 2x5min in PBS-T before incubation in avidin-biotin complex (PK-6100, Vector Labs), as directed. Sections were washed 2x5 min in PBS-T and once in Tris buffer (pH 8.0) for 5 min. Sections were incubated in DAB mixture (SK-4100, Vector Labs) per manufacturer's instruction for exactly 1.5 min before immediate solution removal and washing with Milli-Q followed by 2x5min PBS-T washes. Sections were mounted and dried overnight at RT. The next day, sections were submerged 2x5min in xylene (Fisher Scientific) and coverslipped with DPX mounting medium (06522, Sigma-Aldrich). Slides were imaged with an Aperio VERSA slide scanning microscope (Leica) at 10X magnification.

For immunofluorescent staining, antigen retrieval was accomplished with Tris buffer, pH 8.0 (46-031-CM, Corning; microwaved until boiling) applied to brain sections for 5 min. Next, sections were washed 2x5min in PBS-T, and blocked for non-specific binding in a solution of 5% Normal Donkey Serum (017000121, Jackson Immuno), 0.2% Triton-X (Millipore Sigma) in PBS for 1 hr at RT. After blocking, sections were washed 2x5min in PBS-T before incubating in M.O.M. blocking buffer (1 drop M.O.M. IgG/4ml PBS-T) (MKB-2213-1, Vector Labs) for 1 hr at RT, washed 2x5min in PBS-T and stained overnight at 4°C in a solution of 5% normal donkey serum and PBS-T with the following primary antibodies: APOE (13366, Stem Cell Technologies, 1:500); CD68 (MCA1957, BioRad, 1:200); GFAP (MAB3402, Sigma-Aldrich, 1:800); Iba1 (019-19741, Wako, 1:200); S100β (ab52642, Abcam, 1:200). The next day, sections were washed in 3x5min with PBS-T and incubated in relevant fluorescently-labeled secondary antibodies: (Alexa Fluor; Jackson Immuno Research 1:1000) in PBS-T and DAPI (Thermo Fisher, 1:20,000) for 1 hr at RT. Sections were washed 2x5 min in PBS-T and mounted onto microscopy slides, coverslipped with ProLong Gold mounting medium (P36930, Vector Labs), and sealed with clear nail polish. Slides were imaged with an Aperio VERSA slide scanning microscope (Leica) at 10X magnification or a FV3000 confocal laser scanning microscope (Olympus) at 20X or 40X.

For all analyses measuring immunostaining as percent area coverage of a region of interest, regions were manually drawn in Fiji (ImageJ)[69] and set to a standard threshold value predetermined for each stain. Analyses were conducted via automated ImageJ macros to the extent possible. Analysts drawing regions of interest and setting standard threshold values were blinded to sample to exclude possibility of bias. Categorization of the p-Tau staining type was performed manually, and analysts were blinded to sample.

Volumetric analysis. Every tenth coronal brain section spanning the hippocampus was mounted on a microscope slide for each mouse (~7 sections/mouse, 30µm thick, 300µm apart) and dried for 1 hr at RT. All mounted sections were stained with Sudan black as previously reported[9]. Briefly, mounted sections were stained with 1% Sudan Black in 70% ethanol at RT for 10 min, washed 3 times in 70% ethanol for 5 min, washed 3 times with Milli-Q for 5 min, and coverslipped with ProLong Gold mounting medium. The stained slices were imaged with an Aperio VERSA slide scanning microscope (Leica) at 10X magnification. For hippocampal and lateral ventricle volumetric analyses, regions of interest were drawn Fiji (ImageJ), area measured, and volume was calculated using the formula: volume=(sum of area of all seven sections) x 0.3mm. Quantification encompassed sections roughly between the coordinates AP=-1.2 and AP=-3.4mm. Analysts drawing regions of interest were blinded to sample to exclude possibility of bias.

Dentate gyrus granule cell layer thickness measurement. Two brain sections per mouse (30µm thick, 300µm apart) were stained with NeuN (ABN90, Sigma-Aldrich, 1:500) and imaged with an Aperio VERSA slide scanning microscope (Leica) at 10X magnification as described above. The dentate gyrus granule cell layer thickness was measured manually[9,27]. A line was drawn perpendicular to the NeuN+ cell layer at six locations in two slices in Fiji(ImageJ), and the average was taken for each mouse. Analysts measuring cell layer thickness were blind to sample to exclude possibility of bias.

2.4 Immunocytochemical Analysis of E4-R136S hiPSCs

Immunocytochemistry and image analysis. Cells were plated on 12mm coated glass coverslips in a 24-well plate. Coverslips were coated with hESQ Matrigel (354277, Corning) for hiPSC culture staining or poly-L-lysine and mouse-laminin as described for neuron culture staining prior to plating. Cells were fixed in 4% paraformaldehyde for 15 min, washed 3x5min with 1x DPBS (14080055, Gibco), and permeabilized with 0.5% Triton-X for 5 min followed by 1 hr blocking at RT with 10% Normal Donkey Serum (017000121, Jackson Immuno) and 0.5% Triton-X in PBS. After blocking, cells were stained with primary antibodies overnight at 4°C to the following proteins: human nuclei (ab84680, Abcam, 1:200), MAP2 (AB5622, EMD Millipore, 1:1000), NANOG (09-0020, Stemgent, 1:100), OCT3/4 (sc-5279, SCBT, 1:100), p-Tau [PHF1 (gift from Peter Davies, 1:300)], SOX2 (sc-365823, SCBT, 1:200), total Tau (ab62639, Abcam, 1:800), and TRA-1-60 (MAB4360, EMD Millipore, 1:100). The secondary antibodies were IgG conjugated to Alexa Fluor 488 or Alexa Fluor 594 [against rabbit, mouse or goat IgG (catalog no. A-21206, A-21207, A-21202, A-21203, A-11058, A-11055, from Invitrogen, 1:1500)] Alexa Fluor 647 against rabbit (ab150075, Abcam 1:1500). Coverslips were mounted to microscope slides with VECTASHIELD Prolong Gold with DAPI (H-1200-10, Vector Labs). Images were taken with a FV3000 confocal laser scanning microscope (Olympus) at 20X or 60X. Image analysis to quantify positivity in hiPSC-derived neuron stains was performed using custom macros written in the open-source Fiji (ImageJ) software. For the channels of PHF1 and MAP2 positivity, a standard threshold value was chosen and automatically applied to each channel of each image and total area of immunoreactivity measured. Quantified values reflect area of PHF1:MAP2 ratio.

2.5 Biochemical Analysis

Western blot analysis. Cultured hiPSC-derived neurons were washed with PBS and harvested for Western blot analysis as described[8]. Briefly, neurons were collected in the presence of a high-detergent buffer: 50 mM Tris, 150 mM NaCl, 2% NP-40 (Sigma), 1% sodium deoxycholate, 4% sodium dodecyl sulfate, and supplemented with complete protease inhibitor cocktail pellet

(Roche, 11836145001), phosphatase inhibitor cocktail 2 (P5726, Sigma), phosphatase inhibitory cocktail 3 (P0044, Sigma), and Benzonase® Nuclease (E1014, Sigma-Aldrich). Samples were separated by SDS–PAGE on 12% NuPAGE Bis-Tris polyacrylamide gels (Thermo Fisher Scientific) using MOPS buffer and transferred to nitrocellulose membranes at 18V for 60 min (Trans-Blot Turbo Transfer System, Bio-Rad). The membranes were then blocked in Intercept Blocking Buffer (PBS) (927-70001, LI-COR) for 1 hr at RT and probed with primary antibodies overnight at 4°C to the following proteins: APOE (178479, Sigma-Aldrich, 1:5,000), p-Tau [AT8 (MN1020, Thermo Fisher Scientific, 1:2,000)], p-Tau [PHF1 (gift from Peter Davies, 1:2,000)]. The secondary antibodies were IgG labeled with IRDye 800 or IRDye 680 (LI-COR), including donkey anti-rabbit 680 (926-68073, 1:20,000); donkey anti-mouse 800 (926-32212, 1:20,000); donkey anti-goat 800 (926-32214, 1:20,000). The blotted membranes were scanned with an Odyssey CLx Imaging System (LI-COR). Signals were measured as fluorescence intensity of bands with Image Studio Lite 5.2.5 (LI-COR). Samples were quantified as ratio of target protein to neuronal protein control: APOE:TUJ1, AT8:TUJ1, PHF1:TUJ1, and Tau A12:TUJ1. In some cases, blots were stripped (928-40028, LICOR) and re-probed for antibody of interest and TUJ1 as control.

2.6 Cell Treatments

Low pH buffer wash. hiPSC-derived neurons in a 24-well plate were subjected to a low pH buffer wash as previously described[70]. Briefly, cells were placed on ice and washed 3 times in cold PBS (Gibco) (500µl/well, 30 sec). Cells were then washed twice with 500µl/well cold low pH buffer (0.2M glycine + 0.15M NaCl pH 3.0) for 30 seconds, followed by 2 washes with cold DPBS. Cell lysates were immediately harvested for Western blot analysis. Control wells were placed on ice and underwent equivalent washes with cold PBS instead of low pH buffer.

Long-term treatment of hiPSC-derived neurons with heparin. On day 1, neuronal medium was removed from wells and replaced with fresh complete neuronal medium supplemented with 100µg/ml heparin (H3149, Sigma-Aldrich). On days 2 and 3, heparin was added to wells without

replacing medium to reach 100µg/ml. On day 4, neuronal lysate was collected for Western blot analysis. Control wells underwent equivalent media changes and handling.

2.7 Tau Uptake Assay

Labeling Tau. Recombinant 2N4R Tau was purchased in lyophilized form (AS-55556, AnaSpec). The protein was dissolved into 0.1M Sodium Bicarbonate pH 8.3 and labeled with Alexa Fluor 488 5-SDP Ester (A30052, Invitrogen), mixing for 1 hr at RT following the manufacturer's protocol. After labeling, the proteins were subjected to Zeba Dye and Biotin removal spin columns (A44298, Thermo Scientific) to remove unreacted dye. Degree of labeling (~3.5 mole dye/mole of protein) was determined by obtaining protein concentration by absorbance at 280nm and at 494nm (maximum absorption wavelength for dye) via NanoDrop per Molecular Probes/Invitrogen instructions. Labeled Tau protein was aliquoted and stored at -20°C until use.

Tau uptake assay. Neuronal medium was fully removed, wells were washed with PBS, and fresh complete neuronal medium containing 25nM Tau-488 was added. For heparin competition studies, 100µg/ml heparin (H3149, Sigma-Aldrich) was also added into the medium. Neurons were treated for 1 hr at 37°C. Then, neurons were washed 2 times with PBS to wash out unbound Tau-488. Accutase was used to dissociate and gently lift neurons. Once a near single-cell suspension was achieved, the reaction was quenched with N2B27 medium. Neurons were pelleted by centrifugation, washed with PBS, counted, and resuspended in FACS buffer [1% heat-inactivated FBS, DNAse I (04536282001, Roche, 1:1000)] to $1x10^6$ cells/ml and filtered through 35µm mesh, and DAPI was used to exclude dead cells from analysis. Cells were analyzed using BD LSRFortessa X-20 (BD Biosciences). Each experiment was conducted four times and normalized to E4 neurons without heparin treatment to combine datasets from multiple experiments. Roughly $1x10^5$ to $5x10^5$ events were counted in each experiment. Gating strategy described in **Fig. 4.4**. Control samples of neurons untreated with Tau-488 were included in each experiment to accurately draw Tau-488^- gates in the Live cell population (**Fig. 4.4**) and automatically propagated to all samples in each experiment. Identical experiments to control for

Tau-488 binding versus uptake were conducted at 4°C (**Fig. 4.4**). Flow cytometry data was analyzed using FlowJo v.10.8.0 (BD Biosciences). The Live cell population was down-sampled to 5000 cells to normalize cell number for comparison of the distribution of subpopulations (Tau-488^- and Tau-488^+) across samples.

2.8 Single Cell RNA-seq Analysis of Hippocampal Tissue

Single-nuclei preparation for 10x loading. The mouse hippocampus was dissected on ice and placed into a pre-chilled 2 mL Dounce with 1 mL of cold 1X Homogenization Buffer (1X HB) (250 mM Sucrose, 25 mM KCL, 5 mM $MgCl_2$, 20 mM Tricine-KOH pH7.8, 1 mM DTT, 0.5 mM Sermidine, 0.15 mM Sermine, 0.3% NP40, 0.2 units/µL RNase inhibitor, ~0.07 tabs/ml cOmplete Protease inhibitor). Dounce with "A" loose pestle (~10 strokes) and then with "B" tight pestle (~13 strokes). The homogenate was filtered using a 70 µM Flowmi strainer (Eppendorf) and transferred to a pre-chilled 2 mL LoBind tube (Fischer Scientific). Nuclei were pelleted by spinning for 5 min at 4°C at 350 RCF. The supernatant was removed and the nuclei were resuspended in 400 µL 1X HB. Next, 400 µL of 50% Iodixanol solution was added to the nuclei and then slowly layered with 600 µL of 30% Iodixanol solution under the 25% mixture, then layered with 600 µL of 40% Iodixanol solution under the 30% mixture. The nuclei were then spun for 20 min at 4°C at 3,000RCF in a pre-chilled swinging bucket centrifuge. 200 µL of the nuclei band at the 30%-40% interface was collected and transferred to a fresh tube. Then, 800 µL of 2.5% BSA in PBS plus 0.2 units/µL of RNase inhibitor was added to the nuclei and then were spun for 10 min at 500 RCF at 4C. The nuclei were resuspended with 2% BSA in PBS plus 0.2 units/µL RNase inhibitor to reach at least 500 nuclei/µL. The nuclei were then filtered with a 40 µM Flowmi cell stainer. The nuclei were counted and then ~13,000 nuclei per sample were loaded onto 10x Genomics Next GEM chip G. The snRNA-seq libraries were prepared using the Chromium Next GEM Single Cell 3' Library and Gel Bead kit v3.1 (10x Genomics) according to the manufacturer's instructions. Libraries were sequenced on an Illumina NovaSeq 6000 sequencer at the UCSF CAT Core.

Custom reference genome. The PS19 Tau-P301S transgenic mice carrying knocked-in human APOE isoforms/variant were used for single-nucleus RNA-sequencing (snRNA-seq). The Homo sapiens microtubule associated protein Tau (MAPT) (NCBI Reference Sequence: NM_001123066.4)[71] and the Homo sapiens APOE are genes of interest for this study. These genes are not expected to be a part of the mouse reference genome, so to quantify the reads aligning to these genes of interest, a custom mouse reference genome was made using the reference mouse genome sequence (GRCm38) from Ensembl (release 98)[72] and the mouse gene annotation file from GENCODE (release M23)[73], similar to those used in 10x Genomics Cell Ranger mouse reference package mm10 2020-A. The headers of the Ensembl reference mouse genome sequence fasta file with the chromosome names were modified to match the chromosome names in a fasta file from GENCODE. The annotation GTF file contains entries from non-polyA transcripts that overlap with the protein coding genes. These reads are flagged as multi-mapped and are not counted by the 10x Genomics Cell Ranger v7.0.0 count pipeline[74]. To avoid this, the GTF file was modified to (1) remove version suffixes from transcript, gene, and exon ids to match the Cell Ranger reference packages, (2) remove non-polyA transcripts. The Homo sapiens MAPT sequence and Homo sapiens APOE sequence were appended as separate chromosomes to the end of the mouse reference genome sequence and the corresponding gene annotations were appended to the filtered mouse reference gene annotation GTF file. The 10x Genomics Cell Ranger v7.0.0 mkref pipeline was used to build the custom reference genome using the modified fasta and GTF file.

Pre-processing and clustering of mouse snRNA-seq samples. The snRNA-seq samples included a total of 16 samples with four mice from each of the four genotype groups (PS19-E3, PS19-E4, PS19-E4-S/S, and PS19-E4-R/S). Each group of four mice had two male and two female mice. The demultiplexed fastq files for these samples were aligned to the custom mouse reference genome (See custom reference genome methods for additional descriptions) using the 10x Genomics Cell Ranger v7.0.0 count pipeline[74], as described in the Cell Ranger

documentation. The include-introns flag for the count pipeline was set to true to count the reads mapping to intronic regions. One PS19-E3 sample had low total number of cells, and these cells had relatively large percent of mitochondrial reads (0.1% versus 0.04% for the other samples), thus did not pass the quality control assessment. This sample was therefore excluded from all further analyses.

The filtered count matrices generated by the Cell Ranger count pipeline for 15 samples were processed using the R package for single-nucleus analysis Seurat v4.1.1[75]. Each sample was pre-processed as a Seurat object and the top 1% of cells per sample with a high number of unique genes, cells with <=200 unique genes, and cells >=0.25% mitochondrial genes were filtered out for each sample. The 15 samples were merged into a single Seurat object and normalization and variance stabilization was performed using sctransform[76] with the "glmGamPoi" (Bioconductor package version 1.6.0) method[77] for initial parameter estimation.

Graph-based clustering was performed using the Seurat v4.1.1 functions FindNeighbors and FindClusters. First, the cells were embedded in a k-nearest neighbor (KNN) graph (with k=20) based on the Euclidean distance in the PCA space. The edge weights between two cells were further modified using Jaccard similarity. Next, clustering was performed using the Louvain algorithm implementation in the FindClusters Seurat function. Clustering with 15 PCs and 0.7 resolution resulted in 38 distinct biologically relevant clusters, which was used for further analyses.

Cell type assignment. Data visualization using Seurat v4.1.1 in the UMAP space for the 15 samples revealed no batch effects by age, sex, genotype, date of birth, or nuclear isolation date. The marker genes for each cluster were identified using the FindAllMarkers Seurat function on the SCT assay data. This algorithm uses the Wilcoxon Rank Sum test to iteratively identify differentially expressed genes in a cluster against all the other clusters. Marker genes were filtered to keep only positively expressed genes, detected in at least 25% of the cells in either population and with at least 0.5 log2 fold change. We assigned identities to cell clusters by matching the cell

clusters to known cell types with the expression of canonical cell-type-specific genes, the expression of genes identified in publicly available mouse hippocampal single-cell RNA-seq datasets, and the expression of each cluster's marker genes in a publicly available resource of brain-wide in situ hybridization images, as we reported previously[27].

Subclustering of astrocytic and microglial sn-RNA-seq data. The hippocampal cell clusters 13 and 36 were annotated as the astrocyte cells and hippocampal cell clusters 17 and 19 were annotated as the microglial cells. Both these cell types were further sub-clustered. Normalization and variance stabilization was performed using sctransform[76] with the "glmGamPoi" (Bioconductor package version 1.6.0) method[77] for initial parameter estimation. Graph-based clustering was performed using the Seurat v4.1.1 functions FindNeighbors and FindClusters. First, the cells were embedded in a k-nearest neighbor (KNN) graph (with k=20) based on the Euclidean distance in the PCA space. The edge weights between two cells were further modified using Jaccard similarity. Next, clustering was performed using the Louvain algorithm implementation in the FindClusters Seurat function. Sub-clustering with 15 PCs and 0.9 resolution resulted in 12 distinct biologically relevant subclusters for astrocytes. Sub-clustering with 15 PCs and 0.9 resolution resulted in 15 distinct biologically relevant microglia subclusters.

Gene-set enrichment analysis. Differentially expressed genes between clusters of interest were identified using FindMarkers Seurat function on the SCT assay data. This algorithm uses the Wilcoxon Rank Sum test to identify differentially expressed genes between two populations. Differentially expressed (DE) genes were limited to genes detected in at least 10% of the cells in either population and with at least 0.1 log2 fold change. Volcano plots with log2 fold change and p-value from the differentially expressed gene lists were generated using the EnhancedVolcano R package version 1.14.0. Over-representation (or enrichment) analysis was performed using clusterProfiler v4.2.2[78] to find gene sets of size at least 10 genes in the KEGG database[79] for mouse associated with the DE genes. The p-values are based on a hypergeometric test and are

adjusted for multiple testing using the Benjamini-Hochberg method[80]. The same method was used for gene-set enrichment analysis of astrocyte subclusters and microglia subclusters.

Association between clusters and genotype. A Generalized Linear Mixed-Effects Model to assess association with Animal Models (GLMM_AM) was implemented in the lme4 (v1.1-30) R package[81] and used to estimate the associations between cluster membership and the mouse model. These models were run separately for each cluster of cells. The GLM model was performed with the family argument set to the binomial probability distribution and with the '*nAGQ*' parameter set to 10 corresponding to the number of points per axis for evaluating the adaptive Gauss-Hermite approximation for the log-likelihood estimation. Cluster membership of cells by sample was modeled as a response variable by a 2-dimensional vector representing the number of cells from the given sample belonging to and not belonging to the cluster under consideration. The corresponding mouse id from which the cell was derived was the random effect variable and the animal model for this mouse id was included as the fixed variable. The reference animal model was set to PS19-E4. The resulting p-values for the estimated log odds ratio across the four animal models (with respect to the PS19-E4) and clusters were adjusted for multiple testing using the Benjamini-Hochberg method[80]. The same method was used for estimating the between cluster association with genotype for astrocyte subclusters and microglia subclusters. The proportion of cells from a sample in a given cluster were calculated by adding a pseudo count of 0.01 to the number of cells from a sample in a given cluster and dividing by the total number of cells from a sample. These proportion values were plotted as a boxplot grouped by genotype.

Association between proportion of cell types and histopathological parameters. A Generalized Linear Mixed-Effects Model to assess association with histopathology (GLMM_histopathology) was implemented in the lme4 (v1.1-27.1) R package[81] and used to identify cell types whose proportions are significantly associated with changes in histopathology across the samples. These models were performed separately for each combination of the cluster of cells and the six histological parameters: hippocampal volume (mm^3), the percent of AT8

coverage area, the percent of Iba1 coverage area, the percent of CD68 coverage area, the percent of GFAP coverage area, and the percent of S100β coverage area. The GLM model was performed with the family argument set to the binomial probability distribution family and with the '*nAGQ'* parameter set to 1 corresponding to a Laplace approximation for the log-likelihood estimation. Cluster membership of cells by sample was modeled as a response variable by a 2-dimensional vector representing the number of cells from the given sample belonging to and not belonging to the cluster under consideration. The corresponding mouse model from which the cell was derived was included as a random effect and further the mouse id within the given mouse model was modeled as a random effect as well. Note, this represents the hierarchical nature of this data for the GLMM, and the mouse models are first assumed to be sampled from an "universe" of mouse models, this is then followed by sampling mice within each mouse model. The modeling choice of including the mouse model as a random effect as opposed to a fixed effect is meant to increase the degrees of freedom (or maximize the statistical power) to detect the association of interest, particularly in light of the relatively small number of replicates (3-4) per animal model. The histological parameter under consideration was modeled as a fixed effect in this model.

We selected a subset of cell types of interest and visualized the logOdds ratio estimates (derived from the GLMM fits) in a heatmap using *pheatmap* package 1.0.12 after adjusting the p-values distribution across histopathological parameters across cell types with *Benjamini-Hochberg* multiple testing correction[80]. We applied the pipeline to the astrocyte and microglia subtypes and visualized the associations between astrocyte and microglia subtypes of interest and the histopathological parameters. We estimated the first 5 principal component coordinates using the six logOdds ratio for unit change of the histopathological parameters for each of the cell types and astrocyte and microglia sub-cell types of interest. This was implemented using *prcomp(scale=T, center=T)* in *stats* R package. We visualized the first two PCs using fviz_pca_ind() implemented in factoextra 1.0.7 R package.

2.9 Statistical Analyses

Sample sizes for PS19-E mouse and hiPSC studies were chosen on the basis of estimates to provide statistical power of ≥ 80% and alpha of 0.05 based on preliminary data. Unless explicitly stated, all mouse and cell culture data are shown as mean ± S.E.M. The variances between groups were unequal in most measurements as shown by Bartlett's test, thus Welch's one-Way ANOVA with Dunnett's T3 test was used for multiple comparisons[82,83]. For group-wise statistics on hiPSC-derived neurons measuring the effects of both genotype and heparin treatment or low pH wash, two-ANOVA with Tukey's post hoc test was used for multiple comparisons. $P < 0.05$ was considered to be significant, and all significant P values were included in Figures or noted in Figure legends. Statistical significance was calculated with GraphPad Prism 9 for Mac (GraphPad Software).

CHAPTER III: THE R136S MUTATION PROTECTS AGAINST APOE4-DRIVEN TAU PATHOLOGY, NEURODEGENERATION, AND NEUROINFLAMMATION IN A TAUOPATHY MOUSE MODEL

3.1 Rationale

The differential contributions of APOE isoforms to Tau pathology, neurodegeneration, and neuroinflammation have been of great interest in recent years, yet the underlying mechanisms remain incompletely understood. The discovery of this AD-protective APOE-R136S mutation raises a fundamental question as to whether the R136S mutation can also protect against APOE4-driven pathologies in late-onset AD.

To study if and how the R136S mutation overcomes E4-driven detrimental effects, we utilized PS19-E4, PS19-E3, PS19-E4-S/S, and PS19-E4-R/S mice. We showed that the R136S mutation robustly protects against APOE4-driven AD pathologies and presented potential mechanisms underlying these effects in mouse hippocampi.

3.2 Generation of APOE4-R136S Mice on PS19 Background

As a first step to determine if the R136S mutation also protects against the detrimental effects of APOE4 in late-onset AD, we generated homozygous and heterozygous human APOE4-R136S knock-in mice (**Fig. 3.2a** and **Fig. 3.1a–d**), referred to as E4-S/S-KI and E4-R/S-KI mice, respectively. We used CRISPR/Cas-9-mediated gene editing to introduce the R136S mutation into the *APOE4* locus in human APOE4 knock-in (E4-KI) mice that were previously generated in our lab[56]. Genomic DNA sequencing verified on-target gene editing of R136 to S136 in APOE4 (**Fig. 3.1d**) and found no changes within the top predicted potential off-target sites (**Fig. 3.1e**).

E4-S/S-KI mice were characterized for APOE expression by immunohistochemistry. Immunostaining for APOE and glial fibrillary acidic protein (GFAP) revealed that APOE was primarily expressed in astrocytes in E4-S/S-KI mice (**Fig. 3.1f**), identical to that seen in the parental E4-KI mice (**Fig. 3.1f**). For detailed APOE expression characterization, see single-nucleus RNA-sequencing (snRNA-seq) analysis below.

Reduced Tau pathology was a critical feature of the reported human case with resistance to autosomal dominant early-onset AD whereas amyloid pathology was exceedingly high in this subject[41,48]. Thus, we cross-bred the APOE4 and APOE4-R136S mice with a tauopathy mouse

model, PS19[55], to study the effects of the R136S mutation *in vivo* under a tauopathy setting. Four groups of mice with different APOE genotypes, PS19-E4, PS19-E4-S/S, and PS19-E4-R/S, and PS19-E3 (as control), were used in this study. All mice were analyzed at an average age of 10 months to allow for the development of key AD pathologies: Tau pathology, neurodegeneration, and gliosis[9].

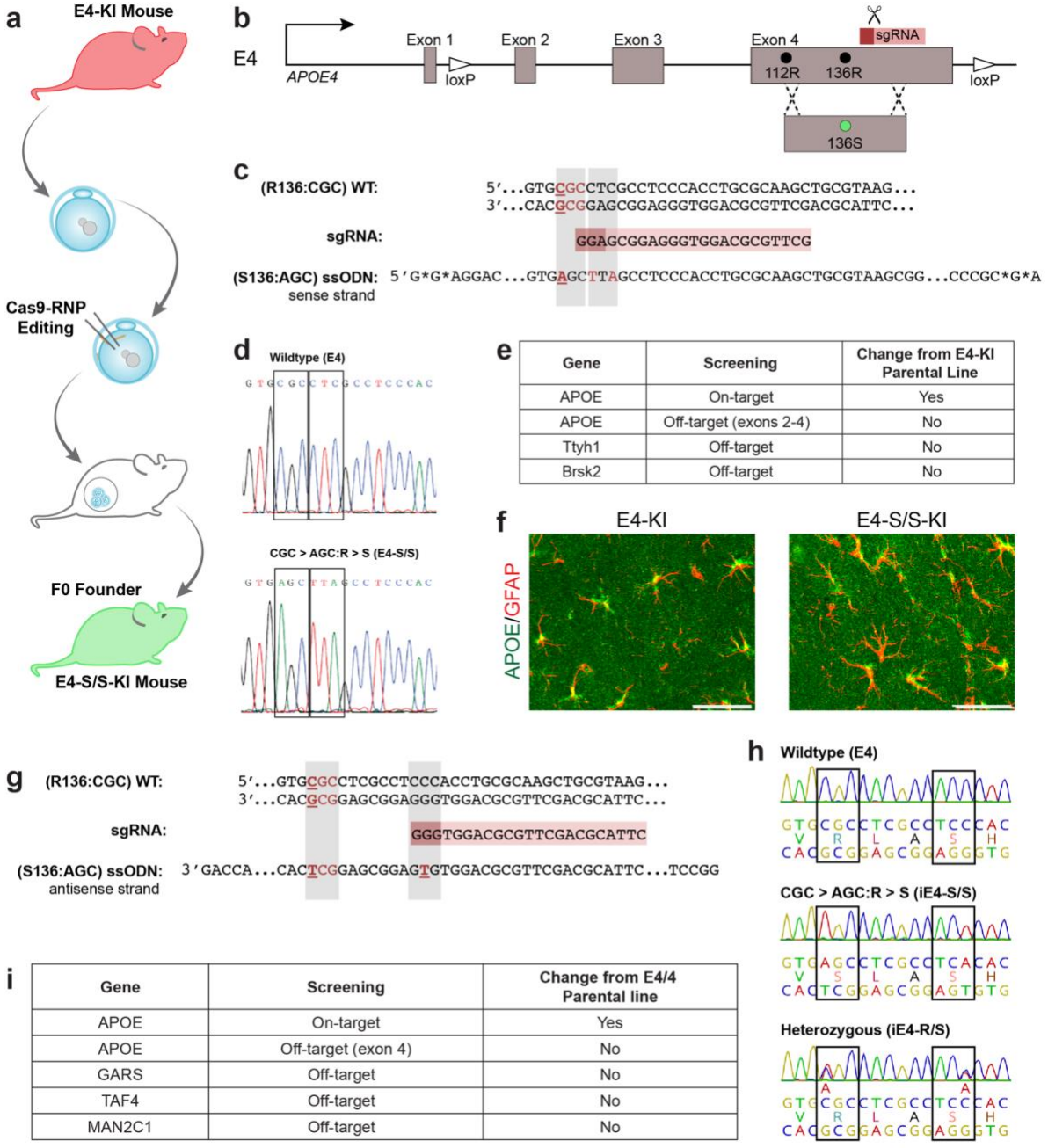

Gene	Screening	Change from E4-KI Parental Line
APOE	On-target	Yes
APOE	Off-target (exons 2-4)	No
Ttyh1	Off-target	No
Brsk2	Off-target	No

Gene	Screening	Change from E4/4 Parental line
APOE	On-target	Yes
APOE	Off-target (exon 4)	No
GARS	Off-target	No
TAF4	Off-target	No
MAN2C1	Off-target	No

Figure 3.1. Generation of human APOE4-R136S knock-in mice and APOE4-R136S hiPSC lines by CRISPR/Cas-9-mediated gene editing.

a, Schematic of generating human APOE4-R136S knock-in (E4-S/S-KI) mice using CRISPR/Cas-9-mediated gene editing. **b**, Schematic of gene editing strategy to generate the R136S mutation in human E4-KI mice and to generate APOE4-R136S (E4-S/S) hiPSCs. **c**, DNA sequences of WT human *APOE4* loci encoding for R136, designed sgRNA, and single-stranded oligodeoxynucleotides donor repair template encoding for S136 and silent mutation at PAM site for generating E4-S/S-KI mice. **d**, Sanger DNA sequencing of WT E4 and E4-S/S at and near the site encoding for residue 136 in E4-S/S-KI mice. **e**, Summary of on-target R136S editing in APOE4 and potential off-target mutation screening for knock-in mice. **f**, Representative

immunofluorescent images of APOE (green) and GFAP (red) in CA1 hippocampal subfield in E4-KI and E4-S/S-KI mice at 12 months of age. **g**, DNA sequences of WT *APOE4* loci encoding for R136, designed sgRNA, and single-stranded oligodeoxynucleotides donor repair template encoding for S136 and silent mutation at PAM site for generating E4-S/S hiPSC lines. **h**, Sanger DNA sequencing of WT E4, E4-S/S, and E4-R/S at and near the site encoding for residue 136. **i**, Summary of on-target R136S editing in APOE4 and potential off-target mutation screening in hiPSC lines. WT, wildtype; sgRNA, single guide RNA; ssODN, single-stranded oligodeoxynucleotide.

3.3 Homozygous R136S Mutation Reduces APOE4-Driven Tau Pathology

With these new tauopathy mouse models, we first examined levels of Tau pathology in the hippocampus by AT8 staining as a measure of phosphorylated Tau (p-Tau) accumulation. PS19-E4 mice displayed roughly two-fold higher AT8 coverage area than PS19-E3 mice (**Fig. 3.2b,c**), in line with the findings from a previous study[9]. Remarkably, PS19-E4-S/S mice exhibited drastically reduced p-Tau accumulation, roughly to the levels in PS19-E3 mice (**Fig. 3.2b,c**). This reduction was not seen in PS19-E4-R/S mice (**Fig. 3.2b,c**), suggesting the protection of APOE4-driven p-Tau accumulation in the hippocampus of mice requires the homozygous R136S mutation.

Distinct p-Tau staining patterns were evident in the hippocampi of the PS19-E mice with different APOE genotypes. Previous studies utilizing mice expressing both human APOE4 and human Tau-P301S have described similar types of p-Tau staining as functions of progressive Tau pathology and association with neurodegeneration[9,13]. With some variation, we observed similar categories of p-Tau staining (**Fig. 3.2d**): Type 1 displays AT8 positivity in mossy fibers and hilus with occasional sparse CA3 and somatic staining; Type 2 has additional dense, tangle-like staining in dentate gyrus granule cells, some staining in CA3 pyramidal cells, and sparse neurite staining in the CA1 region; Type 3 shows further staining in the stratum radiatum of the CA region, primarily neurite staining, with dense staining in only some of the soma; Type 4 has further staining over the entire hippocampus.

Unsurprisingly, the most advanced Type 4 p-Tau staining was enriched in PS19-E4 mice (**Fig. 3.2e**). In fact, roughly 90% of sections analyzed showed Type 3 or Type 4 p-Tau staining in PS19-E4 mice. The early p-Tau staining Types 1 and 2 were enriched in PS19-E3 mice (**Fig. 3.2e**), as seen previously[9]. The PS19-E4-S/S mice displayed the lowest fraction of Type 4 p-Tau staining (~10%) and showed similar levels of enrichment of Types 1 and 2 p-Tau staining to PS19-E3 mice (**Fig. 3.2e**). Notably, the heterozygous R136S mutation was not sufficient to reduce to similar p-Tau staining types as found in PS19-E3 mice. The PS19-E4-R/S mice still showed

roughly 90% Type 3 or 4 p-Tau staining (**Fig. 3.2e**). There was a slight preference for Type 3 over Type 4 p-Tau staining in PS19-E4-R/S mice compared to PS19-E4 mice, possibly indicating a slight slowing of APOE4-driven p-Tau pathological progression with heterozygous R136S mutation in later stages of the disease. Taken together, these data indicate that homozygosity of the R136S mutation is required to effectively protect against APOE4-drived p-Tau accumulation and progression of p-Tau staining patterns in this tauopathy mouse model.

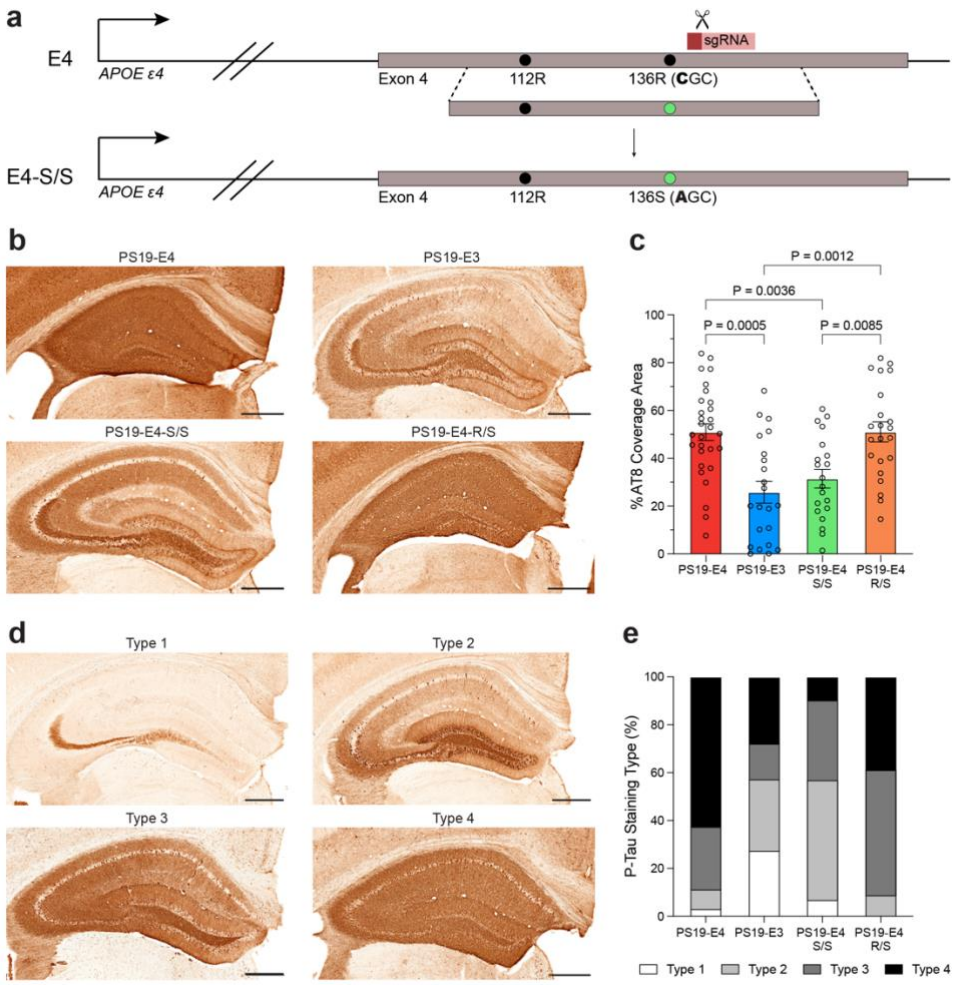

Figure 3.2. Homozygosity of R136S mutation rescues APOE4-promoted Tau pathology in tauopathy mice.

a, Schematic of CRISPR/Cas-9-mediated gene editing strategy to generate human APOE4-R136S knock-in mice. **b**, Representative images of p-Tau immunostaining in hippocampus of 10-month-old PS19-E4, PS19-E3, PS19-E4-S/S, and PS19-E4-R/S mice with the AT8 monoclonal antibody. **c**, Quantification of the percent of AT8 coverage area in the hippocampus (PS19-E4, n=29; PS19-E3, n=22; PS19-E4-S/S, n=20; PS19-E4-R/S, n=22). **d**, Representative images of four AT8 staining patterns in the hippocampus. **e**, Distribution of four p-Tau staining patterns in the hippocampus of 10-month-old PS19-E4, PS19-E3, PS19-E4-S/S, and PS19-E4-R/S mice (PS19-E4, n=61; PS19-E3, n=47; PS19-E4-S/S, n=42; PS19-E4-R/S, n=44 individual brain sections). Scale bars in b and d, 500 μm. Throughout, data are expressed as mean ± s.e.m. Differences between groups were determined by Welch's ANOVA followed with Dunnett T3 multiple comparison test; comparisons of P≤0.05 were labeled on graph.

3.4 The R136S Mutation Ameliorates APOE4-Driven Neurodegeneration

In addition to limited Tau tangle burden, previous reports of a PSEN1-mutation carrier with the APOE3-R136S mutation also described protection from other AD pathologies, including neurodegeneration and neuroinflammation[41,48,49]. These pathologies can also be exacerbated in the presence of APOE4 in late-onset AD[6,9,84]. Thus, we sought to further determine if the R136S mutation could also protect against APOE4-promoted neurodegeneration and neuroinflammation in PS19-E mice.

We first evaluated the extent of neurodegeneration in 10-month-old PS19-E mice with different APOE genotypes. PS19-E4 mice exhibited significantly reduced hippocampal volume compared to PS19-E3 mice (**Fig. 3.3a,b**), as reported previously[9]. Strikingly, PS19-E4-S/S mice had hippocampal atrophy rescued to levels similar to those seen in PS19-E3 mice (**Fig. 3.3a,b**). We also observed a partial rescue of hippocampal atrophy in PS19-E4-R/S mice toward PS19-E3 levels (**Fig. 3.3b**). In another measure of neurodegeneration, PS19-E4 mice displayed significantly enlarged lateral ventricles compared to PS19-E3 mice, and this was protected in PS19-E4-S/S mice (**Fig. 3.3a,c**). Again, the PS19-E4-R/S mice had a partial rescue toward PS19-E3 mice (**Fig. 3.3c**). Analysis of correlation between the APOE4-R136S copy number (0, 1, or 2) and the average of hippocampal volume or the average of posterior lateral ventricle volume revealed a clear gene dose-dependent effect of the R136S mutation on the protection of APOE4-promoted hippocampal neurodegeneration (**Fig. 3.3d,e**).

In PS19-E4 mice, the AT8 (p-Tau) percent coverage area was negatively correlated to hippocampal volume (**Fig. 3.3f**), as shown previously[9], indicating a deleterious role of p-Tau in neurodegeneration. Interestingly, this relationship between p-Tau coverage area and hippocampal volume disappeared in PS19-E3 and PS19-E4-S/S mice, but was still present in PS19-E4-R/S mice (**Fig. 3.3g–i**). This suggests that the lack of protection against p-Tau pathology in PS19-E4-R/S mice (**Fig. 3.2c**) could be a contributing factor to the reduction in hippocampal volume compared to PS19-E3 mice.

We also assessed neurodegeneration by measuring the thickness of the NeuN positive granule cell (GC) layer of the dentate gyrus (DG) (**Fig. 3.3j**). PS19-E3 and PS19-E4-S/S mice showed a significant increase (~20%) in DG GC layer thickness over the PS19-E4 mice (**Fig. 3.3k**). Again, PS19-E4-R/S mice showed a trend, but not significant, increase (12%) in DG GC layer thickness over PS19-E4 mice. Taken together, these data indicate that the R136S mutation ameliorates APOE4-driven neurodegeneration in a gene dose-dependent manner in the tauopathy mice, with the homozygous APOE4-R136S mutation being required for a full rescue to the levels seen in PS19-E3 mice.

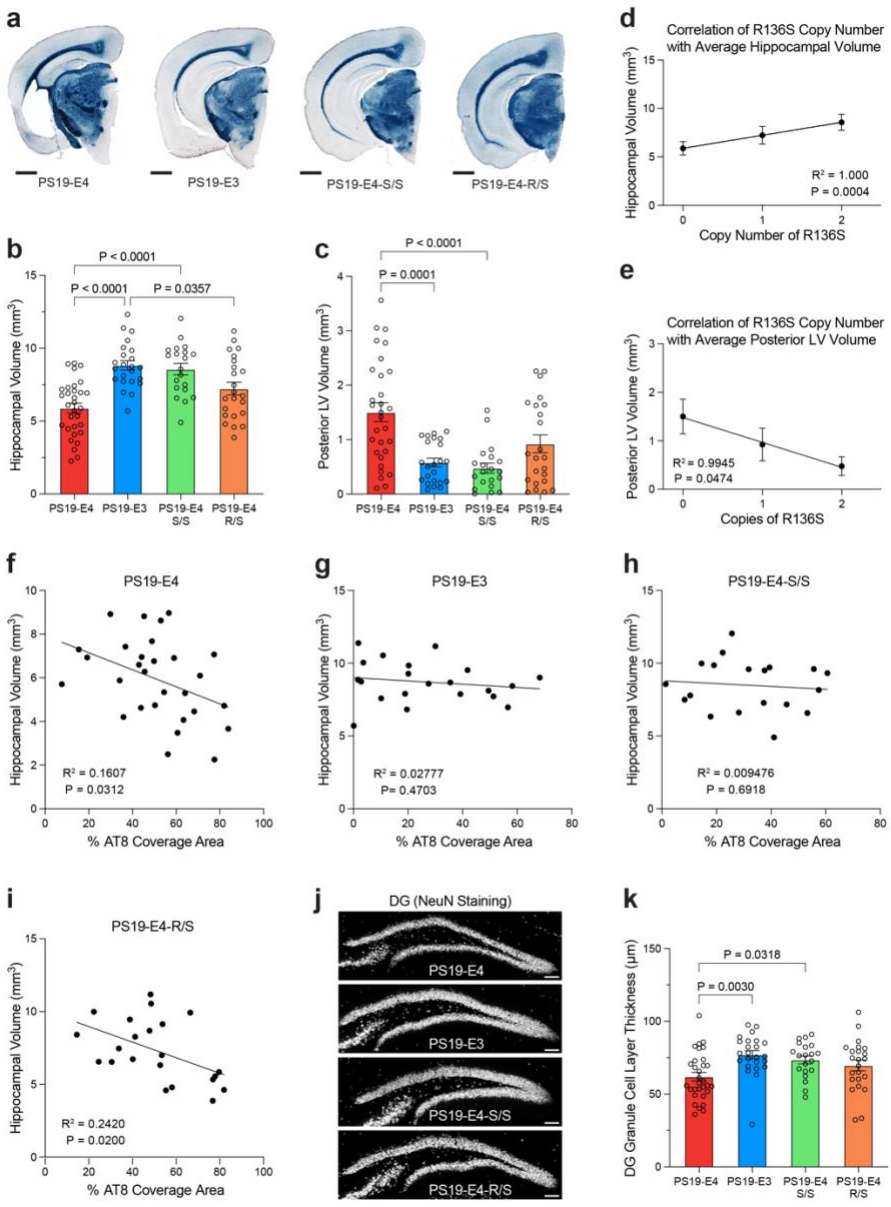

Figure 3.3. The R136S mutation ameliorates APOE4-driven neurodegeneration in tauopathy mice.

a, Representative images of 10-month-old PS19-E4, PS19-E3, PS19-E4-S/S, and PS19-E4-R/S mouse brain sections stained with Sudan black to enhance hippocampal visualization (scale bar, 1 mm). **b**,**c**, Quantification of hippocampal volume (PS19-E4, n=31; PS19-E3, n=23; PS19-E4-S/S, n=20; PS19-E4-R/S, n=23) (b) and posterior lateral ventricle volume (PS19-E4, n=30; PS19-E3, n=23; PS19-E4-S/S, n=20; PS19-E4-R/S, n=23) (c). **d,e**, Correlation of the APOE4-R136S copy number with the average of hippocampal volume (PS19-E4, n=31; PS19-E3, n=23; PS19-E4-S/S, n=20; PS19-E4-R/S, n=23) (d) or the average of posterior lateral ventricle volume (PS19-E4, n=30; PS19-E3, n=23; PS19-E4-S/S, n=20; PS19-E4-R/S, n=23) (e) in PS19-E4 mice with 0, 1, or 2 copies of the R136S mutation. **f–i**, Correlations between % AT8 coverage area and hippocampal volume in PS19-E4 (n=29) (f), PS19-E3 (n=21) (g), PS19-E4-S/S (n=19) (h), and PS19-E4-R/S (n=22) (i) mice. **j**, Representative images of the dentate gyrus (DG) stained for

NeuN in 10-month-old PS19-E4, PS19-E3, PS19-E4-S/S, and PS19-E4-R/S mice (scale bar, 100 μm). **k**, Quantification of DG granule cell layer thickness in PS19-E4 (n=30), PS19-E3 (n=23), PS19-E4-S/S (n=20), and PS19-E4-R/S (n=23) mice. Throughout, data are expressed as mean ± s.e.m. except for correlation plots with 95% CI. Differences between groups were determined by Welch's ANOVA followed with Dunnett T3 multiple comparison test; comparisons of $P \leq 0.05$ were labeled on graph. Pearson's correlation analysis (two-sided). LV, lateral ventricle. DG, dentate gyrus.

3.5 The R136S Mutation Reduces APOE4-Driven Astrocytosis and Microgliosis

Since it has been suggested that glial cells drive degeneration in this tauopathy model[13], we tested whether the R136S mutation protects against APOE4-driven gliosis. We first assessed hippocampal astrocytosis via immunostaining of GFAP and S100β, common markers of total and activated astrocytes, respectively. PS19-E4 mice displayed the highest hippocampal GFAP coverage area, and both PS19-E3 and PS19-E4-S/S mice had drastically reduced GFAP coverage area versus PS19-E4 mice (**Fig. 3.4a,b**). Although PS19-E4-R/S mice also showed a significant reduction in GFAP coverage area compared to PS19-E4 mice, they still had significantly higher GFAP coverage area than PS19-E4-S/S mice (**Fig. 3.4b**). Similar results were obtained for quantifications of S100β coverage area (**Fig. 3.4e,f**), which is a marker of astrocyte reactivity. Thus, the R136S mutation protects against APOE4-driven astrocytosis in a clear gene dose-dependent manner in this tauopathy model.

Importantly, both GFAP and S100β coverage areas inversely correlated with hippocampal volume in PS19-E4 mice (**Fig. 3.4c,g**), suggesting the contribution of astrocytosis to hippocampal degeneration, as reported in a previous study[9]. Strikingly, this correlation was eliminated in PS19-E4-S/S mice (**Fig. 3.4d,h**) and PS19-E3 mice (**Fig. 3.5a,c**), but was preserved in PS19-E4-R/S mice (**Fig. 3.6b,d**), suggesting a gene dose-dependent effect and the need for homozygosity of the R136S mutation to fully protect from APOE4-driven astrocytosis in this tauopathy model.

We next surveyed hippocampal microgliosis via immunostaining of Iba1 (**Fig. 3.4i**), a marker for total microglial population, and CD68 (**Fig. 3.4m**), a marker of activated microglia. The PS19-E4 mice exhibited significantly higher microglia immunoreactivity via measurements of both markers than the PS19-E3, PS19-E4-S/S, and PS19-E4-R/S mice (**Fig. 3.4j,n**). These data indicate that both the homozygous and heterozygous R136S mutation protects against APOE4-promoted microgliosis in the context of tauopathy.

Similar to findings of astrocytosis, both Iba1 and CD68 coverage areas inversely correlated with hippocampal volume in PS19-E4 mice (**Fig. 3.4k,o**), suggesting the contribution

of microgliosis to hippocampal degeneration, as reported in a previous study[9]. By contrast, this correlation was eliminated in PS19-E4-S/S mice (**Fig. 3.4l,p**) and PS19-E3 mice (**Fig. 3.5e,g**). Of note, the percent area coverage of Iba1, but not CD68, was still inversely correlated with hippocampal volume in PS19-E4-R/S mice (**Fig. 3.5f,h**).

In all, these findings indicate that the homozygous and, to a lesser extent, heterozygous R136S mutation strongly protects against APOE4-driven astrocytosis and microgliosis in the context of tauopathy, which consequently can lead to reduced hippocampal neurodegeneration and atrophy.

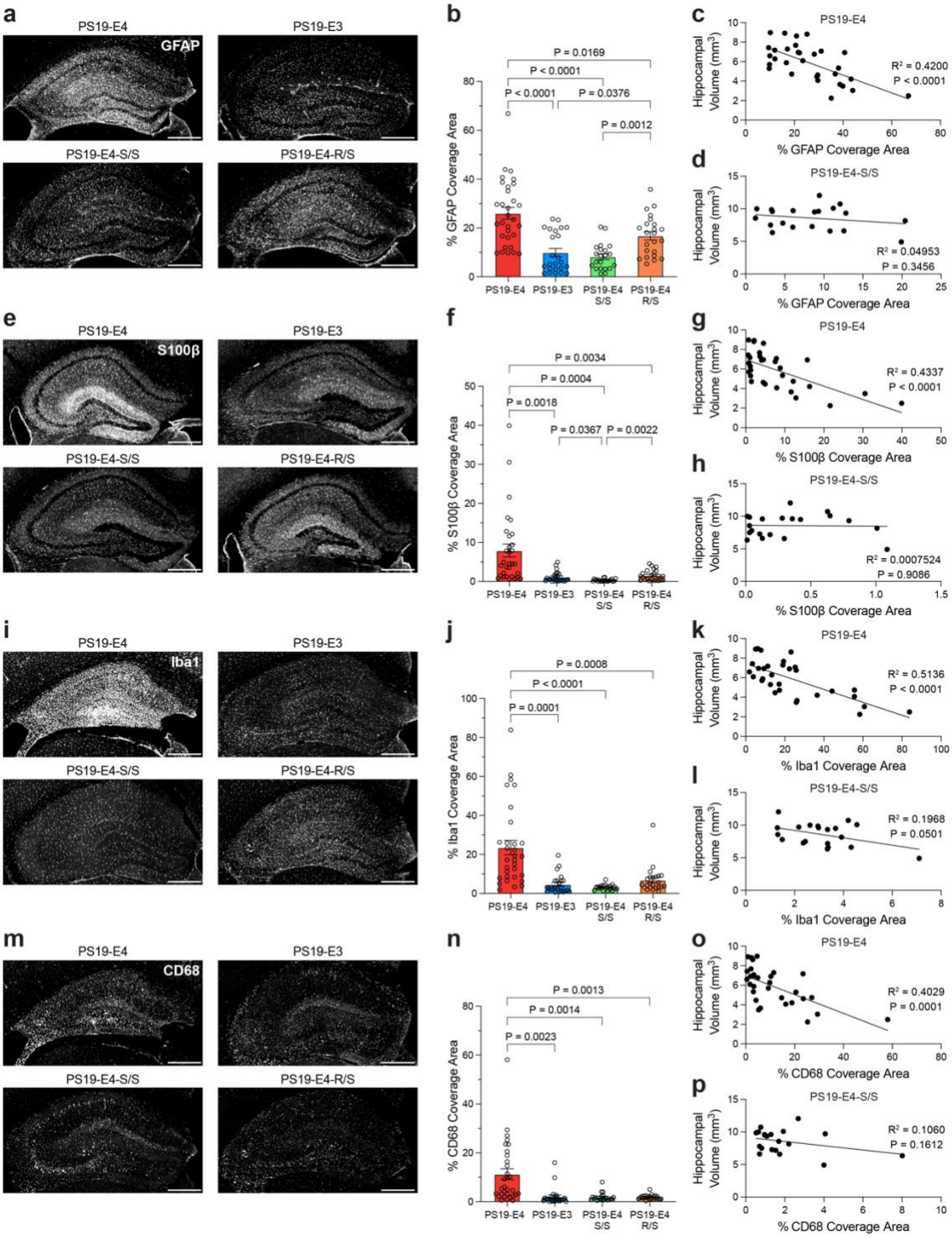

Figure 3.4. The R136S mutation reduces APOE4-driven gliosis in tauopathy mice.
a,b, Representative images of GFAP immunostaining of astrocytes in the hippocampus of 10-month-old PS19-E4, PS19-E3, PS19-E4-S/S, and PS19-E4-R/S mice (a) and quantification of % GFAP coverage area in the hippocampus of these mice (b). **c,d**, Correlations between % GFAP coverage area and hippocampal volume in PS19-E4 (n=31) (c) and PS19-E4-S/S (n=20) (d) mice. **e,f,** Representative images of S100β immunostaining of astrocytes in the hippocampus of 10-

month-old PS19-E4, PS19-E3, PS19-E4-S/S, and PS19-E4-R/S mice (e) and quantification of % S100β coverage area in the hippocampus of these mice (f). **g,h**, Correlations between % S100β coverage area and hippocampal volume in PS19-E4 (n=31) (g) and PS19-E4-S/S (n=20) (h) mice. **i,j**, Representative images of Iba1 immunostaining of microglia in the hippocampus of 10-month-old PS19-E4, PS19-E3, PS19-E4-S/S, and PS19-E4-R/S mice (i) and quantification of % Iba1 coverage area in the hippocampus of these mice (j). **k,l**, Correlation between % Iba1 coverage area and hippocampal volume in PS19-E4 (n=31) (k) and PS19-E4-S/S (n=20) (l) mice. **m,n**, Representative images of CD68 immunostaining of microglia in the hippocampus of 10-month-old PS19-E4, PS19-E3, PS19-E4-S/S, and PS19-E4-R/S mice (m) and quantification of % CD68 coverage area in the hippocampus of these mice (n). **o,p**, Correlations between % CD68 coverage area and hippocampal volume in PS19-E4 (n=31) (o) and PS19-E4-S/S (n=20) (p) mice. For all quantifications in b,f,j,n, PS19-E4, n=31; PS19-E3, n=24; PS19-E4-S/S, n=21; PS19-E4-R/S, n=23. Scale bars are 500 μm. Throughout, data are expressed as mean ± s.e.m. Differences between groups were determined by Welch's ANOVA followed with Dunnett T3 multiple comparison test; comparisons of P≤0.05 were labeled on graph. Pearson's correlation analysis (two-sided).

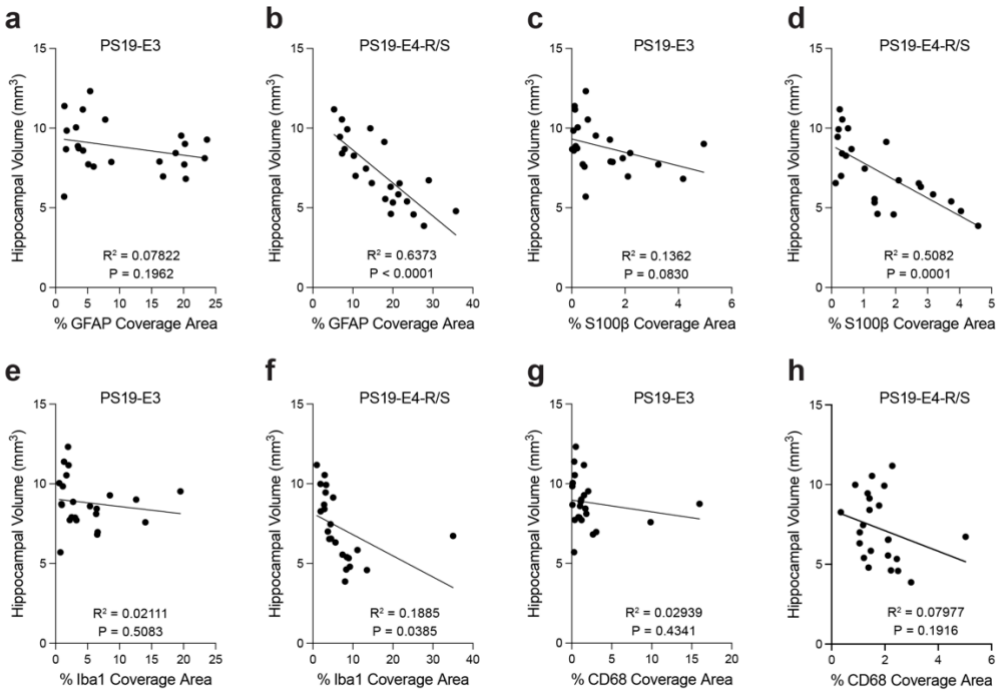

Figure 3.5. Correlations between gliosis and hippocampal volume in PS19-E3 and PS19-E4-R/S mice.

a,b, Correlation between % GFAP coverage area and hippocampal volume in PS19-E3 (a) and PS19-E4-R/S (b) mice. **c,d**, Correlation between % S100β coverage area and hippocampal volume in PS19-E3 (c) and PS19-E4-R/S (d) mice. **e,f**, Correlation between % Iba1 coverage area and hippocampal volume in PS19-E3 (e) and PS19-E4-R/S (f) mice. **g,h**, Correlation between % CD68 coverage area and hippocampal volume in PS19-E3 (g) and PS19-E4-R/S (h) mice. For all correlations in a–h, PS19-E3, n=23; PS19-E4-R/S, n=23. Pearson's correlation analysis (two-sided).

3.6 snRNA-Seq Reveals Protective Effects of the R136S Mutation on APOE4-Driven Neuronal and Oligodendrocytic Deficits

We next evaluated how the R136S mutation might affect the transcriptomic signature of the hippocampus on a cell type-specific level. To this end, we generated snRNA-seq data on isolated hippocampi from 10-month-old PS19-E4, PS19-E3, PS19-E4-S/S, and PS19-E4-R/S mice. The snRNA-seq dataset contained 175,080 nuclei across 26,422 genes after normalization and filtering (**Fig. 3.6**). Unsupervised clustering by the Louvain algorithm[85] and visualization by uniform manifold approximation and projection (UMAP) produced 38 distinct cell clusters (**Fig. 3.7a**). We identified major cell types in the hippocampus based on canonical marker gene expression and identified 21 neuronal clusters, containing 16 excitatory neuron clusters (1, 4, 6-8, 11, 15, 18, 20, 22-24, 26, 28, 30, 33) and five inhibitory neuron clusters (5, 10, 12, 31, 34), and 17 non-neuronal clusters, including three oligodendrocyte clusters (2, 3, 9), two astrocyte clusters (13, 36), two microglia clusters (17, 19) and one oligodendrocyte progenitor cell (OPC) cluster (14) (**Fig. 3.7a**, **Fig. 3.6a,b,** and Supplementary Table 1). As expected, APOE was highly expressed in astrocytes (clusters 13, 36) and to a lesser extent in microglia (clusters 17, 19) in all groups of mice (**Fig. 3.7b** and **Fig. 3.11a,e**). All groups of mice had some neurons and oligodendrocytes also expressing APOE (**Fig. 3.7b**), as we previously reported[27].

To further examine cell type-specific alterations in PS19-E3, PS19-E4-S/S, and PS19-E4-R/S mice versus PS19-E4 mice, we used log odds ratio estimates from a Generalized Linear Mixed Effects Model to assess association with Animal Models (GLMM_AM). We discovered clusters in which there was a significant change in the likelihood that the cluster contained more or fewer cells from PS19-E4-S/S or PS19-E4-R/S mice than from PS19-E4 mice. For example, excitatory neuron clusters 1 (GC) and 6 (CA2/3) had significantly higher odds of containing cells from PS19-E4-S/S mice than from PS19-E4 mice (**Fig. 3.7c,d**, and Supplementary Table 1), suggesting that the homozygous APOE4-R136S mutation promotes the survival of, or protects against APOE4-induced loss of, these neuronal subpopulations. Excitatory neuron clusters 7

(CA2/3) and 28 had significantly higher odds of containing cells from either PS19-E4-S/S or PS19-E4-R/S mice than from PS19-E4 mice (**Fig. 3.7c,d**, and Supplementary Table 1), suggesting that both the homozygous and the heterozygous APOE4-R136S mutation promotes the survival of, or protects against APOE4-induced loss of, these neuronal subpopulations.

We next examined whether the transcriptomic landscapes of the APOE4-R136S-protected neuronal clusters (1, 6, 7, and 28) were altered relative to those expressing APOE4. Analyses of differentially expressed (DE) genes and their enriched Kyoto Encyclopedia of Genes and Genomes (KEGG) pathways in PS19-E4-S/S or PS19-E4-R/S mice versus PS19-E4 mice revealed that the top enriched DE pathways in these clusters were indicative of neuronal health and function, including axon guidance, synaptic integrity, and long-term potentiation for both the homozygous and heterozygous R136S mutation (**Fig. 3.7e,f** for cluster 6, **Fig. 3.8a–f** for clusters 1, 7, 28, and Supplementary Table 1 for clusters 1, 6, 7, 28). This suggests that even heterozygosity of the R136S mutation provides protection against APOE4 effects in these neuronal clusters at the transcriptomic level. Notably, some DE pathways enriched in these clusters did differ based on the R136S gene dose. For example, some neurodegenerative disease related pathways appeared only in the comparison of PS19-E4-R/S versus PS19-E4 mice, and heparin sulfate biosynthesis pathways appeared only in the comparison of PS19-E4-S/S versus PS19-E4 mice (**Fig. 3.7e,f**, **Fig. 3.6c–f**, and Supplementary Table 1). This suggests gene dose-related differential effects of APOE4-R136S mutation on these pathways in some neuronal clusters.

The oligodendrocyte cluster 9 had lower odds of containing cells from PS19-E4-S/S and PS19-E4-R/S mice than from PS19-E4 mice (**Fig. 3.7c,d**, and Supplementary Table 1). Further analyses comparing oligodendrocyte cluster 9 versus 2 revealed enrichment of DE genes and KEGG pathways related to neurodegeneration, including AD (**Fig. 3.7g** and Supplementary Table 1), suggesting that cells in cluster 9 are disease-associated oligodendrocytes (DAOs). Some DE genes recently identified as markers of DAOs in AD mouse models[86] were also upregulated in

cluster 9 versus cluster 2, such as those mediating the inflammatory process (*H2-D1*, *Il33*, and *C4b*) (**Fig. 3.8g**). Additionally, the DAO cluster 9 also had many significantly upregulated genes uniquely identified in the current study, including *Kirrel3*, *Neat1*, *Apod*, *Dgki*, *Fmn1*, *Pex5l*, *Sik3*, and *Grik2* (**Fig. 3.8h**). Interestingly and importantly, many of these highly upregulated DAO genes unique to cluster 9 were drastically downregulated in PS19-E4-S/S mice versus PS19-E4 mice (**Fig. 3.8h,i**). These data indicate not only that the DAO cluster 9 was diminished by the APOE4-R136S mutation, but also that the R136S mutation dramatically reverses the distinct transcriptomic profile of the DAOs.

Given the dramatic protection against AD pathologies observed in the APOE4-R136S tauopathy mice and human neurons, we next tested the potential link between the pathological measurements and the transcriptomic feature-defined cell clusters in this snRNA-seq dataset. Log odd ratio estimates from another GLMM to assess associations with histopathology (GLMM_histopathology) uncovered that the proportion of cells in excitatory neuron clusters 1, 6, 7, and 28 exhibited significant positive associations with hippocampal volume and negative associations with the coverage areas of p-Tau and gliosis (**Fig. 3.7h** and Supplementary Table 2). Conversely, the proportion of DAOs in oligodendrocyte cluster 9 had significant negative association with hippocampal volume and positive association with the coverage areas of p-Tau and gliosis (**Fig. 3.7h** and Supplementary Table 2). Thus, the APOE4-R136S mutation promoted the survival of excitatory neuronal subpopulations (clusters 1, 6, 7, and 28) and the elimination of DAO subpopulation (cluster 9).

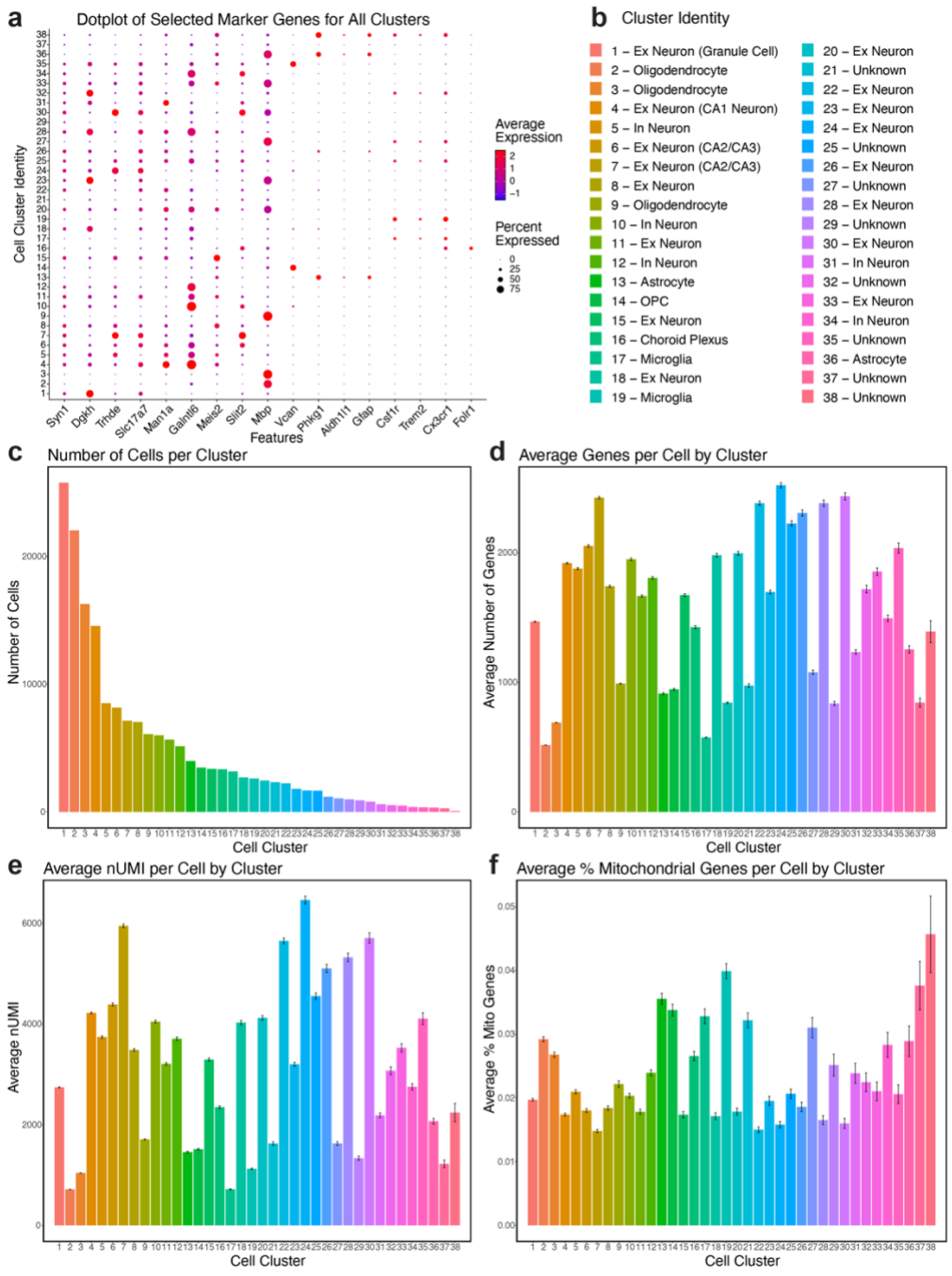

Figure 3.6. Quality control measures in snRNA-seq analysis of tauopathy mice with different APOE genotypes.

a, Dot-plot depicting normalized average expression of selected cell identity marker genes for all 38 distinct hippocampal cell clusters. **b**, Cluster identity of 38 distinct cell types. **c,** The number of cells per cluster. **d,** The average genes per cell in each cluster (± s.e.m). **e,** The average nUMI (unique molecular identified) per cell in each cluster (± s.e.m). **f,** The average % mitochondrial genes per cell in each cluster (± s.e.m). Number of cells (n) for each cell cluster can be found in c. For details of the analyses, see Methods.

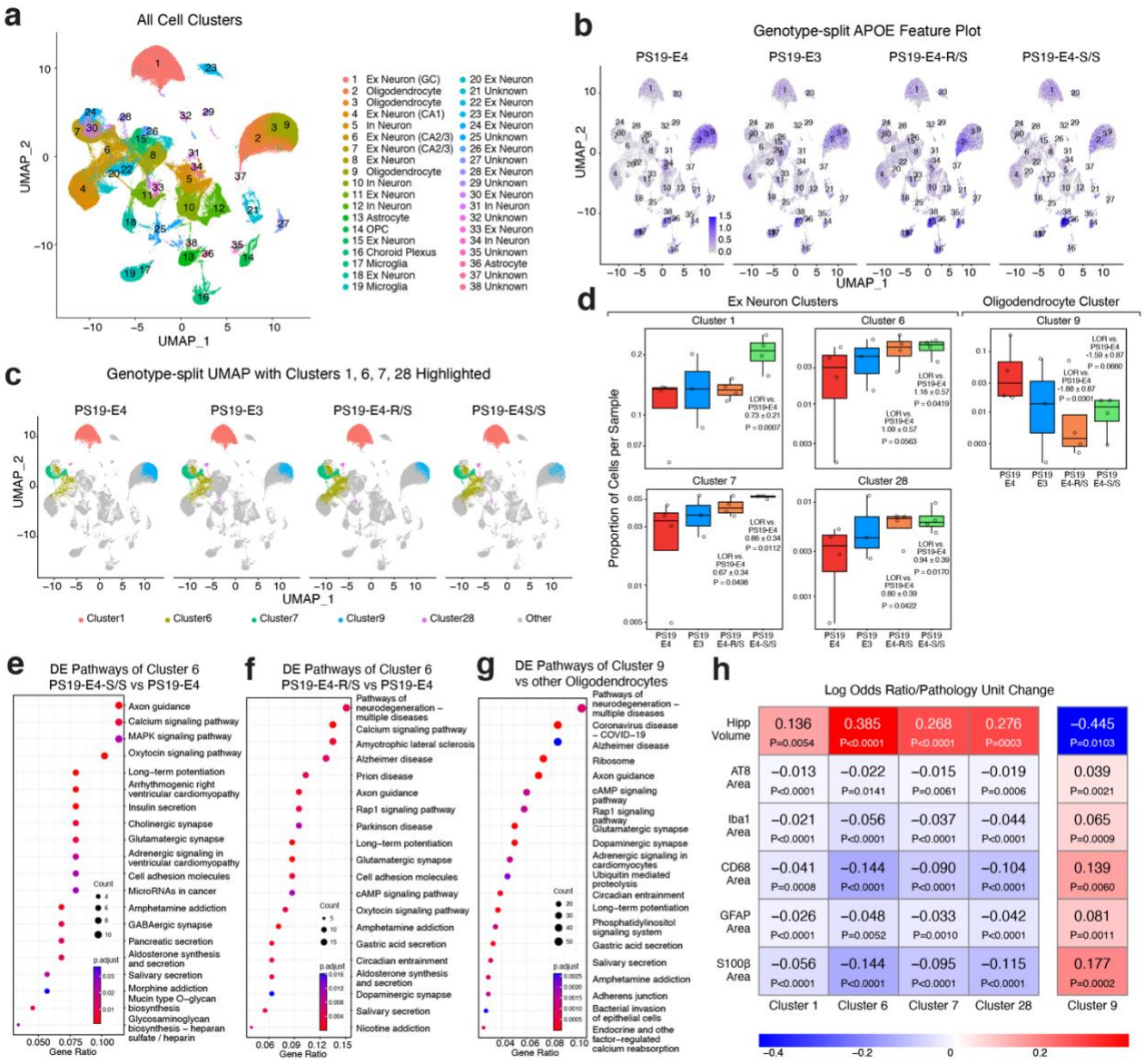

Figure 3.7. snRNA-seq reveals protective effects of the R136S mutation on APOE4-driven neuronal and oligodendrocytic deficits in mice.

a, UMAP projection of 38 distinct cell clusters in hippocampi of 10-month-old PS19-E4 (n=4), PS19-E3 (n=3), PS19-E4-S/S (n=4), and PS19-E4-R/S (n=4) mice. **b**, Feature plot showing relative levels of normalized human APOE gene expression across all 38 hippocampal cell clusters by APOE genotype (PS19-E4, n=4; PS19-E3, n=3; PS19-E4-S/S, n=4; PS19-E4-R/S, n=4). **c**, UMAP projection highlighting hippocampal cell clusters 1, 6, 7, 9, 28 for each genotype group. **d**, Bar plot of the mean estimates of Mean change in log odds estimates of cells per sample of PS19-E3, PS19-E4-R/S, and PS19-E4-S/S mice compared to log odds estimates of cells per sample from PS19-E4 mice for clusters 1, 6, 7, 9, 28. **e**,**f**, KEGG pathway enrichment dot-plot of top 20 pathways significantly enriched for DE genes of neuronal cluster 6 in PS19-E4-S/S (**e**) or PS19-E4-R/S (**f)** versus PS19-E4 mice. P-values are based on a hypergeometric test and are adjusted for multiple testing using the Benjamini-Hochberg method. The size of the dots is proportional to the number of genes in the given gene set. Gene ratio represents the proportion of genes in the respective gene set that are deemed to be differentially expressed using the

FindMarkers function in Seurat. **g**, KEGG pathway enrichment dot-plot of top 20 pathways significantly enriched for DE genes of oligodendrocyte cluster 9 versus oligodendrocyte cluster 2. **h**, Heatmap plot of log odds ratio per unit change in each pathological measurement for clusters 1, 6, 7, 9, 28. The log odds ratio represents the mean estimate of the change in the log odds of cells per sample from a given animal model, corresponding to a unit change in a given histopathological parameter. Associations with pathologies are colored (negative associations, blue; positive associations, red). P-values in d are from fits to a GLMM_AM and p-values in h are from fits to a GLMM_histopathology. All error bars represent s.e.m. Ex Neuron, excitatory neuron; GC, granule cell; In neuron, inhibitory neuron; OPC, oligodendrocyte precursor cell; DE, differentially expressed. For details of the analyses, see Methods.

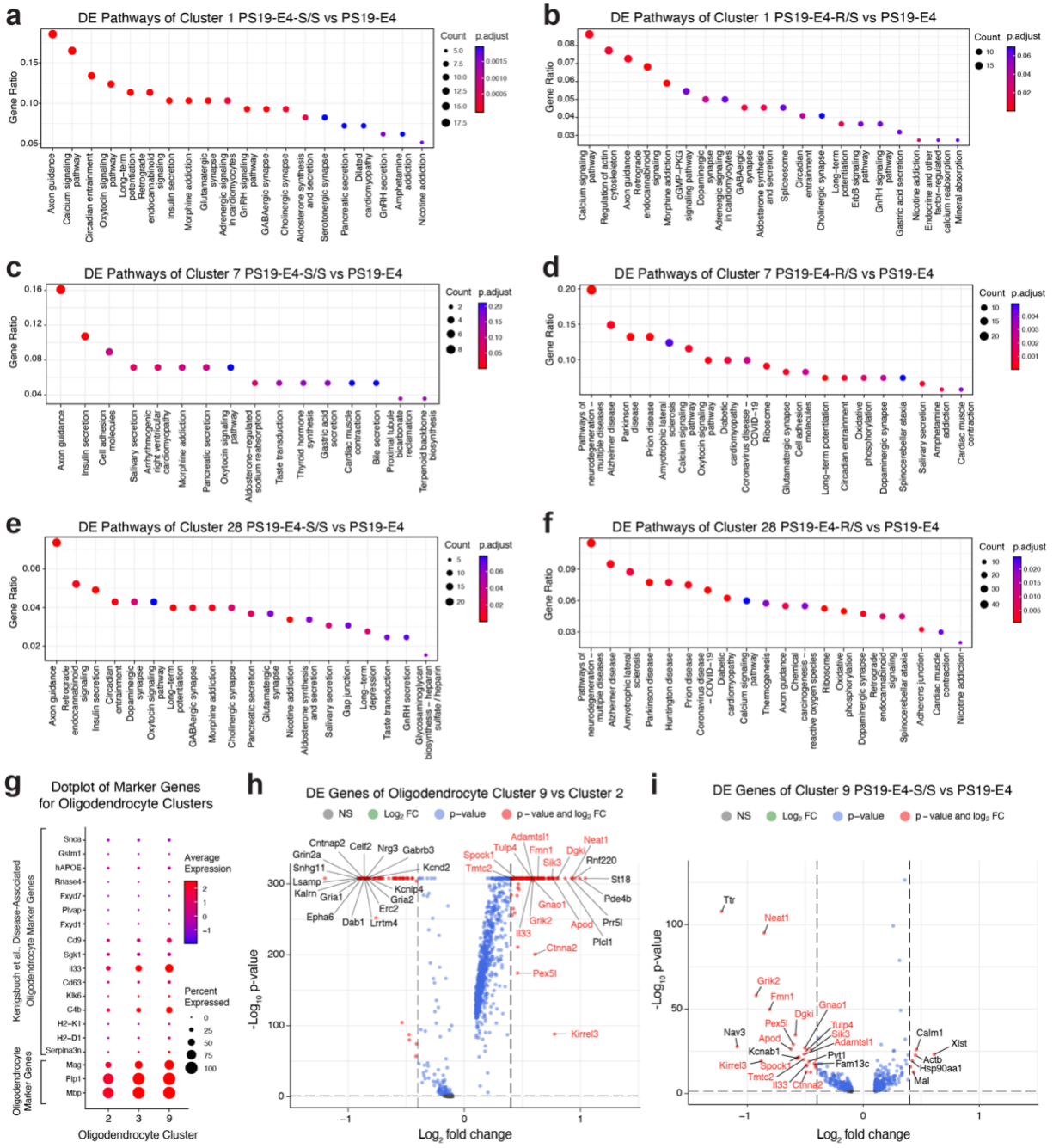

Figure 3.8. snRNA-seq analysis of disease-protective neuronal clusters and disease-associated oligodendrocyte cluster.

a,b, KEGG pathway enrichment dot-plot of top 20 pathways significantly enriched for DE genes of neuronal cluster 1 in PS19-E4-S/S (a) or PS19-E4-R/S (b) versus PS19-E4 mice. P-values are based on a hypergeometric test and are adjusted for multiple testing using the Benjamini-Hochberg method. The size of the dots is proportional to the number of genes in the given gene set. Gene ratio represents the proportion of genes in the respective gene set that are deemed to be differentially expressed using the FindMarkers function in Seurat. **c,d**, KEGG pathway enrichment dot-plot of top 20 pathways significantly enriched for DE genes of neuronal cluster 7

in PS19-E4-S/S (c) or PS19-E4-R/S (d) versus PS19-E4 mice. **e,f**, KEGG pathway enrichment dot-plot of top 20 pathways significantly enriched for DE genes of neuronal cluster 28 in PS19-E4-S/S (e) or PS19-E4-R/S (f) versus PS19-E4 mice. **g**, Dot-plot normalized average expression of selected homeostatic and disease-associated oligodendrocyte (DAO) marker genes for oligodendrocyte clusters 2, 3, and 9. **h**, Volcano plot for top DE genes of oligodendrocyte cluster 9 versus cluster 2. **i**, Volcano plot for top DE genes of oligodendrocyte cluster 9 in PS19-E4-S/S versus PS19-E4 mice. For h,i, horizonal dashed line indicates p-value = 0.05 and vertical dashed lines indicate $\log_2$ fold change = 0.4. DE, differentially expressed; NS, nonsignificant; FC, fold change. For details of the analyses, see Methods.

3.7 The APOE4-R136S Mutation Increases Disease-Protective and Decreases Disease-Associated Astrocyte Subpopulations

Based on our observation that even the heterozygous R136S mutation significantly reduces APOE4-promoted gliosis (**Fig. 3.4**), we further dissected the effects of the APOE4-R136S mutation on subtypes of glial cells by subclustering astrocytes and microglia. Subclustering of astrocytes (clusters 13, 36 in **Fig. 3.7a**) produced 12 astrocyte subpopulations (**Fig. 3.9a**). Log odds ratio estimates from a GLMM_AM showed that astrocyte subcluster 3 was enriched in PS19-E3 and PS19-E4-S/S mice, but not in PS19-E4-R/S mice, compared to PS19-E4 mice (**Fig. 3.9b,c**, and Supplementary Table 3). Log odds ratio estimates also revealed that astrocyte subclusters 5 and 7 had lower odds of containing cells from PS19-E4-S/S mice than from PS19-E4 mice (**Fig. 3.9b,c**, and Supplementary Table 3). In fact, subcluster 7 was almost completely eliminated in PS19-E4-S/S mice (**Fig. 3.9b**). PS19-E4-R/S mice also had a significant decrease in log odds ratio of astrocyte subcluster 7, although to a lesser extent than PS19-E4-S/S mice (**Fig. 3.9b,c**). All of these three astrocyte subclusters (3, 5, and 7) expressed high levels of APOE (**Fig. 3.11a**). DE gene analyses comparing each of these subclusters to all other astrocyte subclusters revealed astrocyte subcluster 3 as homeostatic astrocytes and astrocyte subclusters 5 and 7 as disease-associated astrocytes (DAAs), with upregulation of *Gfap*, *Aqp4*, *Ctsb*, *Vim*, *Serpina3a*, *C4b*, and *Cd9* expression (**Fig. 3.9d** and Supplementary Table 3), similar to those reported previously[87]. Additionally, astrocyte subcluster 5 also had many highly upregulated DE genes uniquely identified in the current study, including *Neat1*, *Pex5l1*, *Nkain2*, *Dgki*, *Magi2*, *Apod*, and *Ank3* (**Fig. 3.9e** and Supplementary Table 3), as compared to other astrocyte subclusters. Likewise, astrocyte subcluster 7 also had many significantly upregulated DE genes uniquely identified in the current study, including *Neat1*, *Ank3*, *Mat2a*, *Nav2*, *Dcun1d4*, *Glis3*, and *Mrsp6* (**Fig. 3.9g** and Supplementary Table 3), as compared to other astrocyte subclusters. Of note, many of these highly upregulated DE genes in the DAA subclusters 5 and 7 were drastically downregulated in PS19-E4-S/S mice versus PS19-E4 mice (**Fig. 3.9f,h** and Supplementary Table

3). DE pathway analyses supported the notion that subcluster 3 comprised homeostatic astrocytes and subclusters 5 and 7 comprised DAAs (**Fig. 3.11b–d** and Supplementary Table 3).

The enrichment of cells in the homeostatic astrocyte subcluster 3 was positively associated with hippocampal volume and negatively associated with the coverage areas of p-Tau and gliosis (**Fig. 3.9i** and Supplementary Table 4), as determined by log odds ratio estimates from GLMM_histopathology. Likewise, the log odds ratio estimates also revealed that enrichments of the DAA subclusters 5 and 7 were negatively associated with hippocampal volume and positively associated with the coverage areas of p-Tau and gliosis (**Fig. 3.9i** and Supplementary Table 4). Together, these findings illustrate that the homozygous APOE4-R136S mutation increases disease-protective homeostatic astrocytes (subcluster 3) and both homozygous and heterozygous APOE4-R136S eliminate DAAs (subclusters 5, 7) in the hippocampus of the tauopathy mice, with homozygous R136S mutation having a greater effect than heterozygous R136S mutation.

To further assess the relationship between the disease-protective and disease-associated astrocyte subpopulations, we applied PCA clustering of neuronal clusters 1, 6, 7, 28 and oligodendrocyte cluster 9 together with astrocyte subclusters 3, 5, 7 against all measured pathologies. Such PCA analysis revealed that the disease protective astrocyte subcluster 3 had a similar contribution to the measured pathologies as the four disease-protective neuronal clusters (1, 6, 7, 28) (**Fig. 3.12**). Likewise, the DAA subclusters 5 and 7 had similar contributions to the measured pathologies as the DAOs (cluster 9) (**Fig. 3.12**). These findings support the notion that APOE4-R136S leads to a significant increase in the disease-protective homeostatic astrocyte subpopulation, likely contributing to the enrichment of neuronal clusters 1, 6, 7, and 28, as well as to a significant reduction in the DAA subpopulations, likely contributing to the elimination of the DAOs.

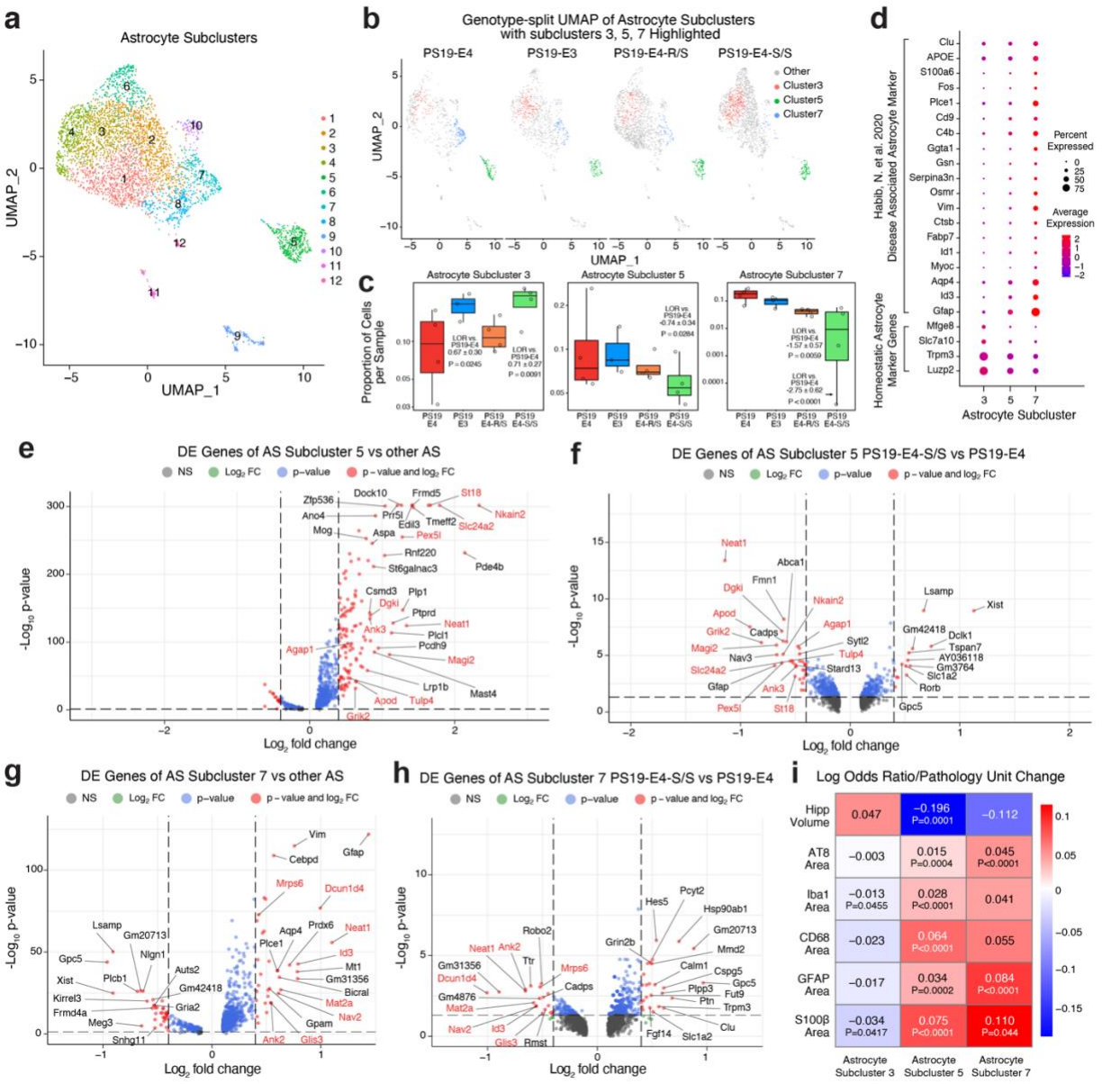

Figure 3.9. The APOE4-R136S mutation increases disease-protective and decreases disease-associated astrocyte subpopulations.

a, UMAP projection of 12 astrocyte subclusters after subclustering hippocampal cell clusters 13 and 36. **b**, UMAP projection highlighting astrocyte subclusters 3, 5, 7 for each genotype group (PS19-E4, n=4; PS19-E3, n=3; PS19-E4-S/S, n=4; PS19-E4-R/S, n=4). **c**, Bar plot of the mean estimates of log odds of cells per sample of PS19-E3, PS19-E4-R/S, and PS19-E4-S/S mice compared to log odds estimates of cells per sample from PS19-E4 mice for astrocyte subclusters 3, 5, 7. **d**, Dot-plot of normalized average expression of selected homeostatic and disease-associated astrocyte (DAA) marker genes for astrocyte subclusters 3, 5, 7. **e**, Volcano plot for top 30 DE genes of astrocyte subcluster 5 versus other astrocyte subclusters. **f**, Volcano plot for top 30 DE genes of astrocyte subcluster 5 in PS19-E4-S/S versus PS19-E4 mice. **g**, Volcano plot for top 30 DE genes of astrocyte subcluster 7 versus other astrocyte subclusters. **h**, Volcano plot for top 30 DE genes of astrocyte subcluster 7 in PS19-E4-S/S versus PS19-E4 mice. **i**, Heatmap plot of log odds ratio per unit change in each pathological measurement for astrocyte subclusters 3,

5, 7. P-values in c are from fits to a GLMM_AM and p-values in i are from fits to a GLMM_histopathology. For e–h, horizonal dashed line indicates p-value = 0.05 and vertical dashed lines indicate $\log_2$ fold change = 0.4. All error bars represent s.e.m. AS, astrocyte; DE, differentially expressed; NS, nonsignificant; FC, fold change. For details of the analyses, see Methods.

3.8 The APOE4-R136S Mutation Increases Disease-Protective and Decreases Disease-Associated Microglial Subpopulations

To investigate alterations in the subpopulation of microglia across APOE genotype groups, we subclustered microglia (clusters 17, 19 in **Fig. 3.7a**) and identified 15 microglial subpopulations (**Fig. 3.10a**). Log odds ratio estimates from GLMM_AM revealed that microglia subclusters 2 and 11 were likely to contain more cells from PS19-E4-S/S mice than from PS19-E4 mice, while microglia subcluster 8 was likely to contain fewer cells from PS19-E4-S/S mice than from PS19-E4 mice (**Fig. 3.10b,c** and Supplementary Table 5). PS19-E4-R/S mice also had a significant decrease in microglia subcluster 8, although to a lesser extent than PS19-E4-S/S mice (**Fig. 3.10b,c** and Supplementary Table 5). Microglia subcluster 8 expressed high levels of APOE, while microglia subclusters 2 and 11 expressed relatively low levels of APOE (**Fig. 3.11e**). DE gene analyses comparing each of these microglia subclusters with all other microglia subclusters identified microglia subclusters 2 and 11 as homeostatic microglia and microglia subcluster 8 as disease-associated microglia (DAMs) (**Fig. 3.10d** and Supplementary Table 5), with downregulation of homeostatic microglial genes and upregulation of DAM genes, similar to those reported previously[88]. Additionally, the DAM subcluster 8 had many highly upregulated DE genes uniquely identified in the current study, including *Igf1*, *Gpnmb*, *Mamdc2*, *Kif13*, and *Sash1* (**Fig. 3.10e** and Supplementary Table 3), as compared to other astrocyte subclusters. Strikingly, these highly upregulated DE genes in the DAM subcluster 8 were heavily downregulated in PS19-E4-S/S mice versus PS19-E4 mice (**Fig. 3.10f** and Supplementary Table 3). Furthermore, DE pathway analysis revealed enrichment of KEGG pathways related to MAPK signaling, cAMP signaling, and synaptic function in microglia subclusters 2 and 11 (**Fig. 3.11f,h**, and Supplementary Table 5), supporting their homeostatic function. Conversely, the DAM subcluster 8 had enrichment in KEGG pathways related to lysosome, autophagy, and various diseases (**Fig. 3.11g** and Supplementary Table 5), supporting its disease association.

To further test whether these three microglia subclusters represent disease-protective and disease-associated microglial subpopulations, we calculated the log odds ratio estimates from GLMM-histology. This analysis revealed that the proportion of cells in microglia subclusters 2 and 11 exhibited positive associations with hippocampal volume and negative associations with the coverage areas of p-Tau and gliosis, while microglia subcluster 8 had a negative association with hippocampal volume and a significant positive association with the coverage areas of p-Tau and gliosis (**Fig. 3.10g** and Supplementary Table 6). In all, these findings indicate that the APOE4-R136S mutation increases disease-protective homeostatic microglia (subclusters 2, 11) and eliminates DAMs (subcluster 8) in the hippocampus of the tauopathy mice, with the homozygous R136S mutation having a greater effect than the heterozygous R136S mutation.

Again, PCA analysis revealed that the disease protective microglia subcluster 2 had similar contribution to the measured pathologies as the four disease-protective neuronal clusters (1, 6, 7, 28) (**Fig. 3.12**). Likewise, the DAM subcluster 8 had a similar contribution to the measured pathologies as the DAOs (cluster 9) (**Fig. 3.12**). These findings again support the notion that APOE4-R136S leads to a significant increase in the disease-protective homeostatic microglia subpopulation, likely contributing to the enrichment of neuronal clusters 1, 6, 7, and 28, as well as to a significant reduction in the DAM subpopulation, likely contributing to the elimination of the DAOs.

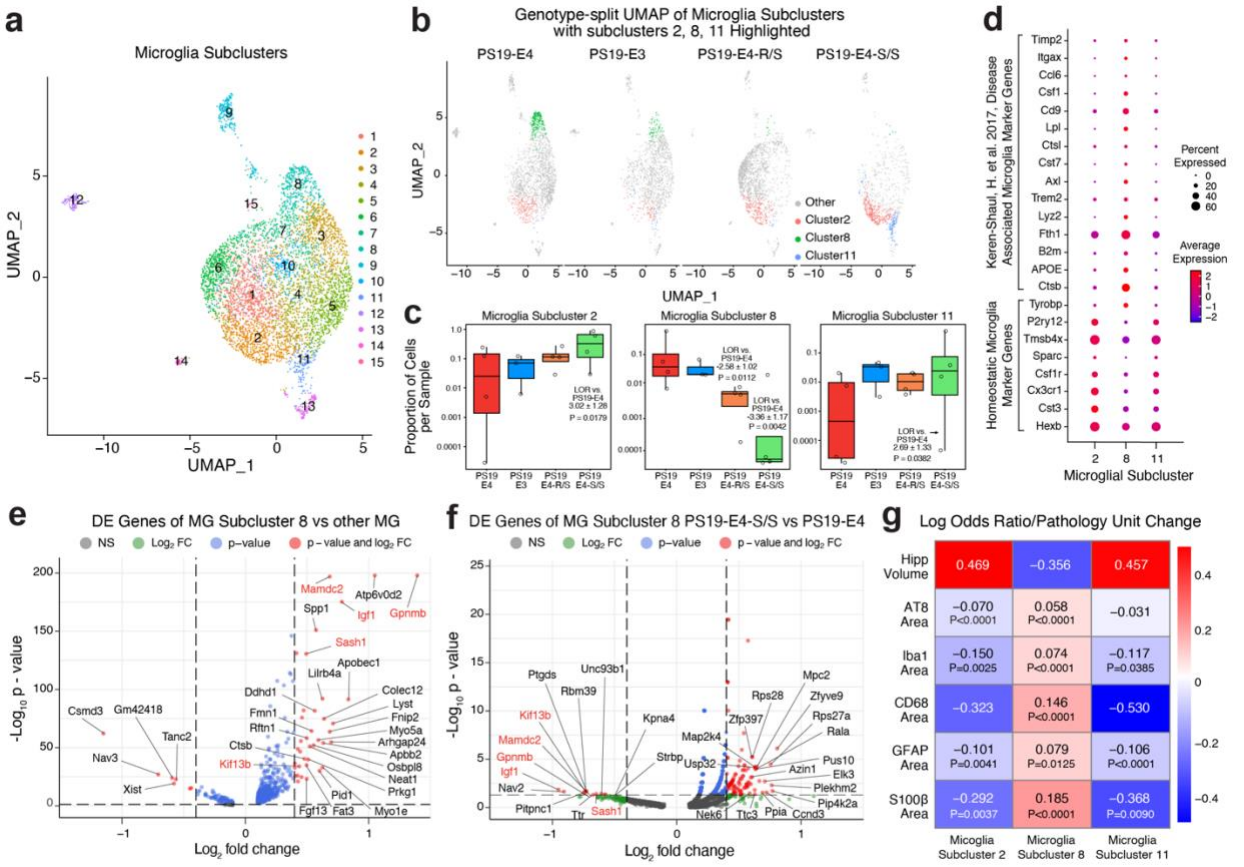

Figure 3.10. The APOE4-R136S mutation increases disease-protective and decreases disease-associated microglial subpopulations.

a, UMAP projection of 15 microglia subclusters after subclustering hippocampal cell clusters 17 and 19. **b**, UMAP projection highlighting microglia subclusters 2, 8, 11 for each mouse genotype group (PS19-E4, n=4; PS19-E3, n=3; PS19-E4-S/S, n=4; PS19-E4-R/S, n=4). **c**, Bar plot of mean estimates of log odds of cells per sample of PS19-E3, PS19-E4-R/S, and PS19-E4-S/S mice compared to log odds estimates of cells per sample from PS19-E4 mice for microglia subclusters 2, 8, 11. **d**, Dot-plot of normalized average expression of selected homeostatic and disease-associated microglia (DAM) marker genes for microglia subclusters 2, 8, 11. **e**, Volcano plot for top 30 DE genes of microglia subcluster 8 versus other microglia subclusters. **f**, Volcano plot for top 30 DE genes of microglia subcluster 8 in PS19-E4-S/S versus PS19-E4 mice. **g**, Heatmap plot of log odds ratio per unit change in each pathological measurement for microglia subclusters 2, 8, 11. P-values in c are from fits to a GLMM_AM and p-values in g are from fits to a GLMM_histopathology. For e,f, horizonal dashed line indicates p-value = 0.05 and vertical dashed lines indicate $\log_2$ fold change = 0.4. All error bars represent s.e.m. MG, microglia; DE, differentially expressed; NS, nonsignificant; FC, fold change. For details of the analyses, see Methods.

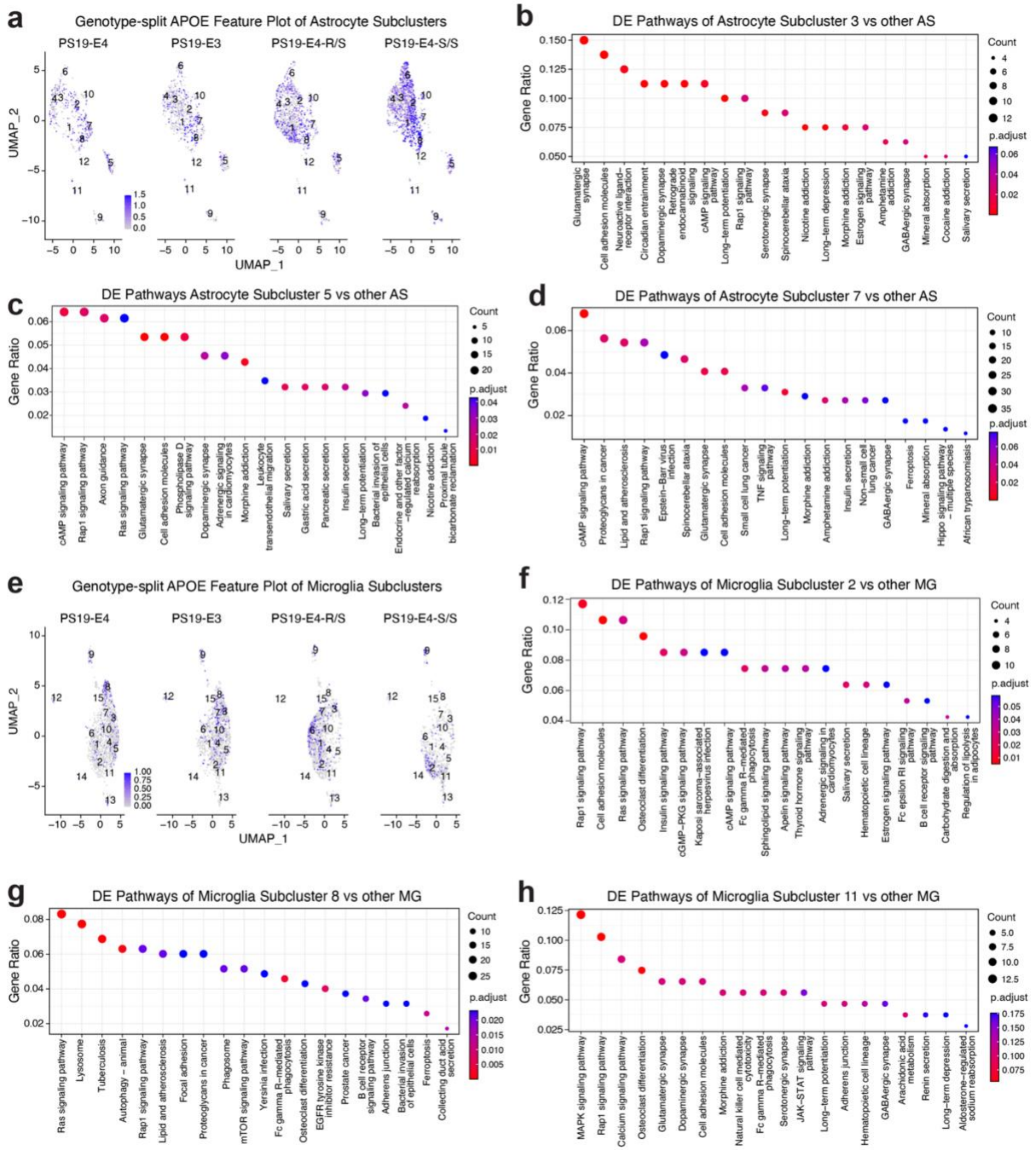

Figure 3.11. snRNA-seq analysis of astrocyte and microglia subclusters.
a, Feature plot showing relative levels of normalized human APOE gene expression across all 12 astrocyte subclusters by APOE genotype. **b–d**, KEGG pathway enrichment dot-plot of top 20 pathways significantly enriched for DE genes of astrocyte subclusters 3 (b), 5 (c), and 7 (d) versus other astrocyte subclusters. P-values are based on a hypergeometric test and are adjusted for multiple testing using the Benjamini-Hochberg method. The size of the dots is proportional to the

number of genes in the given gene set. Gene Ratio represents the proportion of genes in the respective gene set that are deemed to be differentially expressed using the FindMarkers function in Seurat. **e**, Feature plot showing relative levels of normalized human APOE gene expression across all 15 microglia subclusters by APOE genotype. **f–h**, KEGG pathway enrichment dot-plot of top 20 pathways significantly enriched for DE genes of microglia subclusters 2 (f), 8 (g), and 11 (h) versus other microglia subclusters. DE, differentially expressed; AS, astrocyte; MG, microglia. For details of the analyses, see Methods.

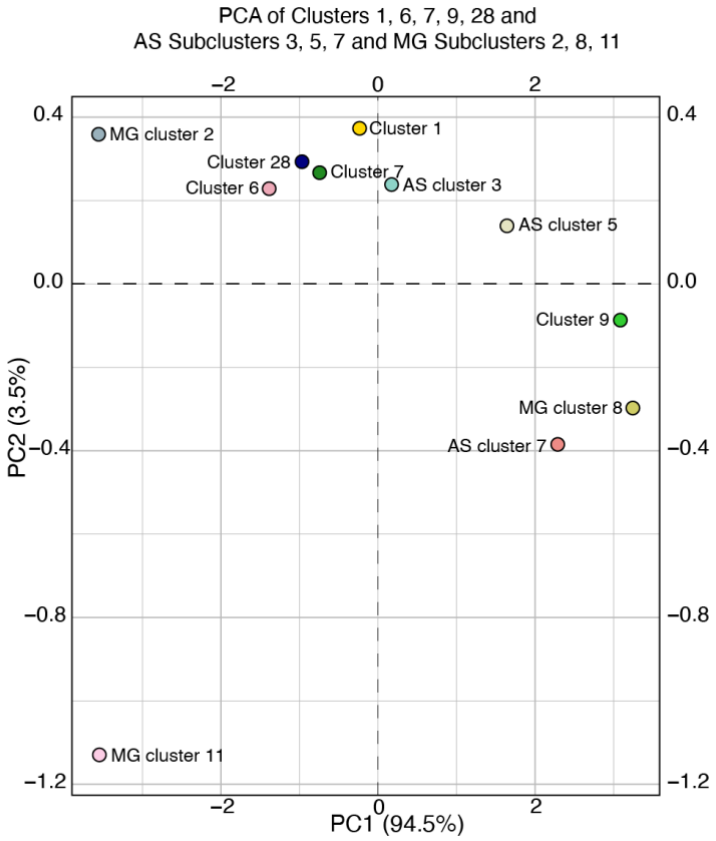

Figure 3.12. PCA clustering of selected hippocampal cell clusters as well as astrocyte and microglia subclusters against all measured pathologies.
Principal component analysis plot for hippocampal clusters 1, 6, 7, 9, 28, astrocyte subclusters 3, 5, 7, and microglia subclusters 2, 8, 11 against all measured pathologies (hippocampal volume and coverage areas of AT8, Iba1, CD68, GFAP, and S100β). PC1 and PC2 showed the overall relationship between clusters based on similarity of the estimated log odds ratio per unit change in six pathologies per cluster/subcluster. AS, astrocyte; MG, microglia. For details of the analyses, see Methods.

CHAPTER IV: THE R136S MUTATION PROTECTS AGAINST APOE4-INDUCED P-TAU ACCUMULATION LIKELY DUE TO REDUCED TAU UPTAKE VIA HSPGS IN HUMAN NEURONS DERIVED FROM APOE4/4 ALZHEIMER'S PATIENT

4.1 Generating Isogenic E4-S/S and E4-R/S hiPSCs From a Patient-Derived E4/4 hiPSC Line

To parse out the mechanisms underlying the protection of the R136S mutation against APOE4-driven Tau pathology, we decided to further model its protective effect in APOE4 hiPSC-derived neurons. A parental APOE4/4 hiPSC line had previously been generated in our lab from an AD patient homozygous for the *APOE4* allele, which provided a human and disease-relevant cellular model[8]. From this APOE4/4 hiPSC line, we generated isogenic hiPSC lines with either the homozygous (E4-S/S) or the heterozygous (E4-R/S) R136S mutation using CRISPR/Cas-9-mediated gene editing (**Fig. 3.1b,g,h**). Genomic DNA sequencing verified genetic editing resulting in the change from R136 to S136 in APOE4 (**Fig. 3.1h**) and found no mutations in the top predicted potential off-target sites (**Fig. 3.1i**).

Five stable, isogenic hiPSC lines (three E4-S/S clones and two E4-R/S clones) were karyotyped to ensure no chromosomal abnormalities. Additionally, they all expressed stem cell marker genes Nanog, OCT3/4, SOX2, and TRA-1-60 (**Fig. 4.1a,b**). hiPSC lines were then differentiated into neurons expressing mature neuronal marker MAP2 (**Fig. 4.1c**), via an optimized method using dual-SMAD inhibition[8,68]. Both the E4-S/S and E4-R/S neuronal cultures showed normal morphology, neurite outgrowth pattern, and viability (**Fig. 4.1c**). We then utilized the following isogenic hiPSC-derived neurons for further analyses: the parental E4 hiPSC line (E4), a previously generated isogenic APOE3 hiPSC line (E3)[8], and the isogenic E4-S/S and E4-R/S hiPSC lines.

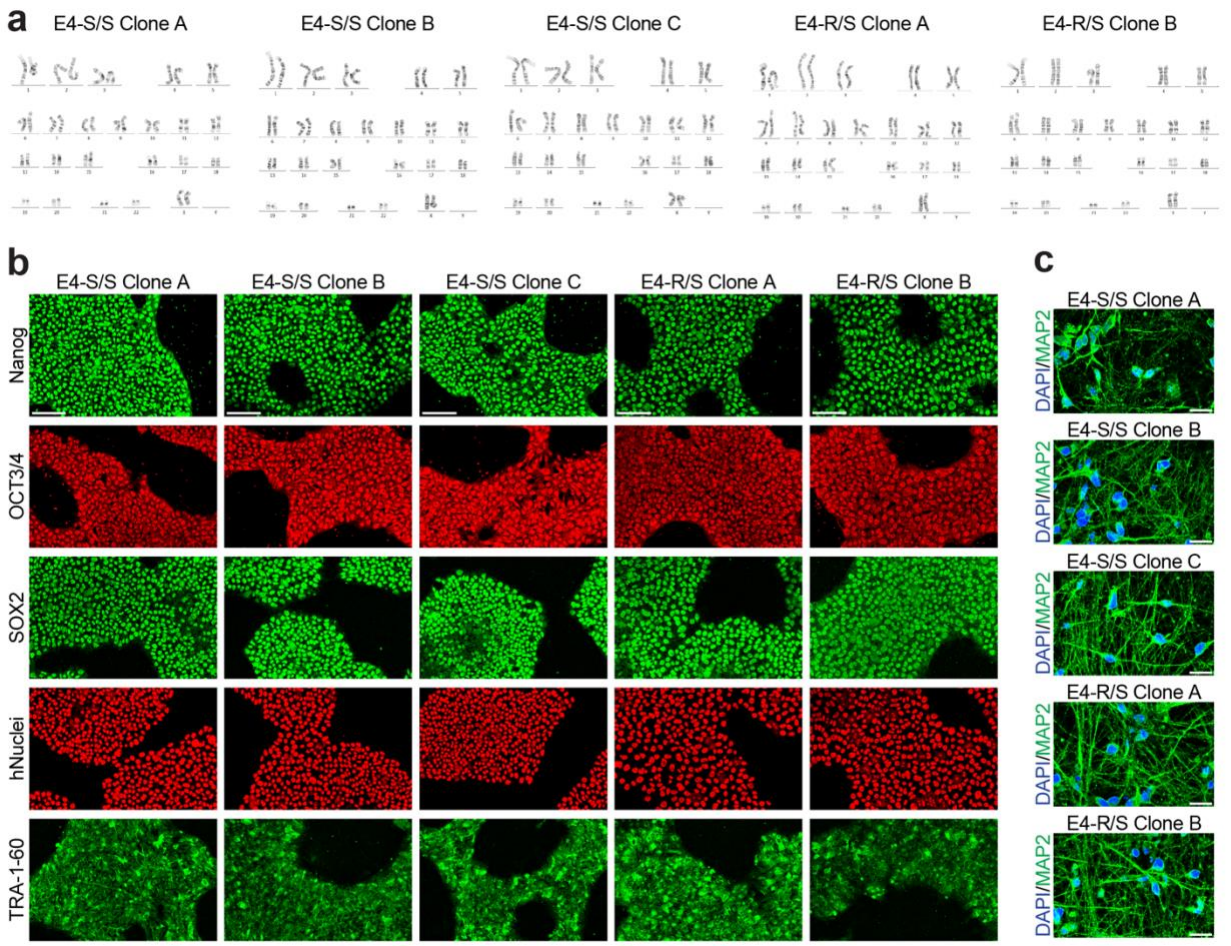

Figure 4.1. Characterization of E4-S/S and E4-R/S hiPSC lines and neuronal differentiation. **a**, Karyogram of E4-S/S-A, E4-S/S-B, E4-S/S-C, E4-R/S-A, and E4-R/S-B hiPSC lines. **b**, Representative immunofluorescent images of pluripotent stem cell markers Nanog, OCT3/4, SOX2, hNuclei, and TRA-1-60 from E4-S/S-A, E4-S/S-B, E4-S/S-C, E4-R/S-A, and E4-R/S-B hiPSC lines. **c**, Representative immunofluorescent images of mature neuronal marker MAP2 (green) and DAPI (blue) in 3-week-old neurons differentiated from E4-S/S-A, E4-S/S-B, E4-S/S-C, E4-R/S-A, and E4-R/S-B hiPSC lines.

4.2 Homozygous R136S Mutation Reduces APOE4-Induced p-Tau Accumulation in hiPSC-Derived Neurons

The effect of R136S mutation in human neurons was first assessed by quantification of APOE levels via Western blotting. Interestingly, the E4-S/S neurons had a remarkable five-fold increase in APOE protein levels compared to E4 neurons (**Fig. 4.2a,b** and **Fig. 4.3a**), likely due to decreased receptor-mediated APOE clearance and degradation caused by the receptor-binding defective R136S mutation[43,89–92]. The E4-R/S neurons did not show such an effect on APOE protein levels (**Fig. 4.2a,b** and **Fig. 4.3a**).

To determine whether the R136S mutation also protects human neurons from APOE4-induced p-Tau accumulation, we analyzed levels of p-Tau by Western blotting. The E3 neurons showed a significant reduction in p-Tau levels compared to E4 neurons, as measured by two widely used p-Tau-specific monoclonal antibodies, PHF1 for phospho-epitope Ser396/Ser404 and AT8 for phospho-epitope Ser202/Thr205 (**Fig. 4.2a,c,d** and **Fig. 4.3b,c**), confirming our previous report[8]. The E4-S/S neurons showed a dramatic ~40% reduction in p-Tau levels compared to E4 neurons at both the combined hiPSC line level (**Fig. 4.2c,d**) and the individual hiPSC line level (**Fig. 4.3b,c**). Notably, E4-R/S neurons did not show the same protection against APOE4-induced p-Tau accumulation (**Fig. 4.2a,c,d** and **Fig. 4.3b,c**).

We additionally measured levels of p-Tau via immunocytochemical staining with the PHF1 monoclonal antibody, which again showed that E4-S/S neurons had ~40% reduction in p-Tau levels compared to E4 neurons (**Fig. 4.2e,f**), while E4-R/S neurons had no such effect (**Fig. 4.2e,f**). We also observed some beading patterns in PHF1+ neurites, suggesting p-Tau aggregates and/or degenerating neurites, which were the least prevalent in E4-S/S neurons (**Fig. 4.2e**, arrows). Taken together, these data illustrate that the homozygous, but not heterozygous, R136S mutation protects against APOE4-induced p-Tau accumulation in human neurons, in line with the observations in PS19-E4-S/S and PS19-E4-R/S mice (**Fig. 3.2**).

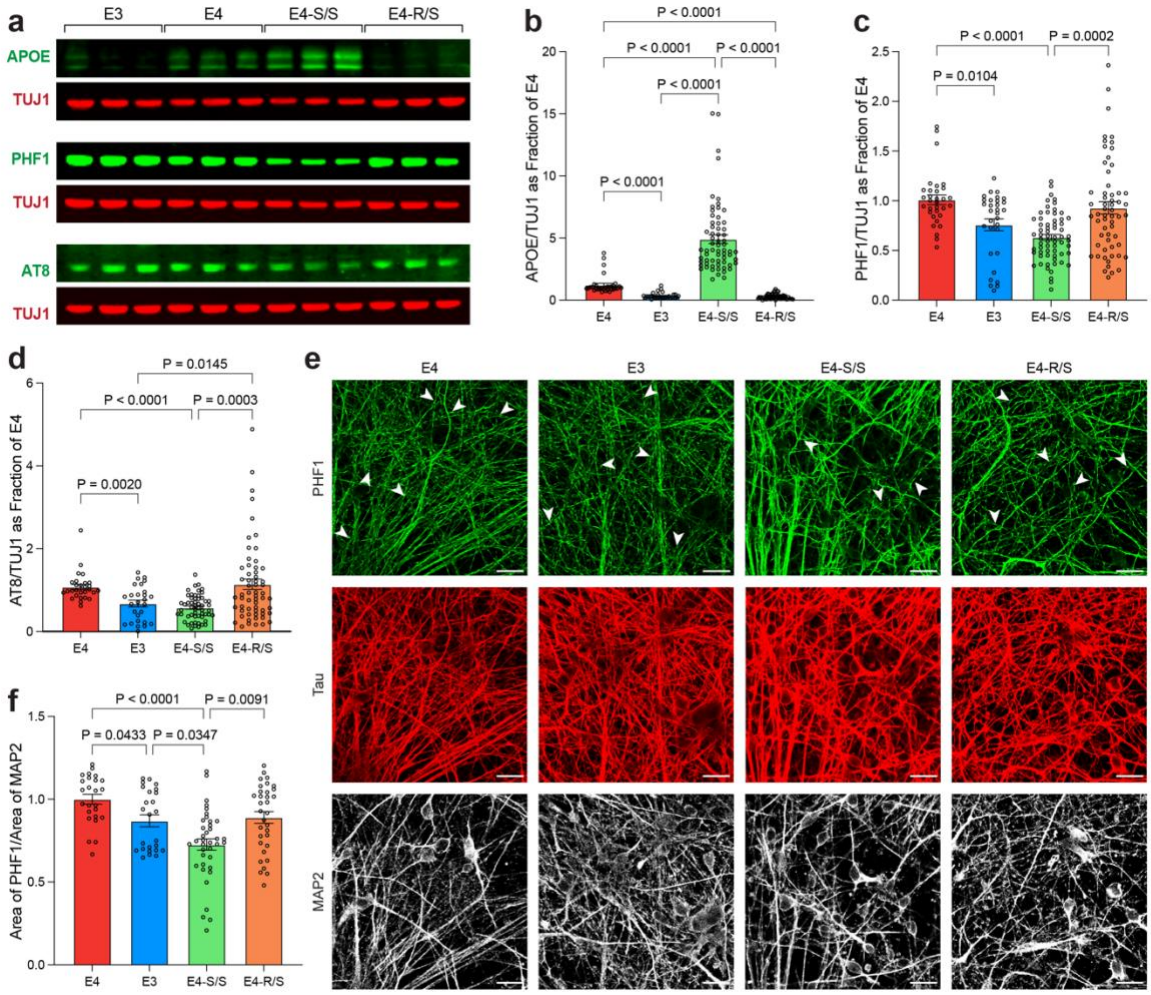

Figure 4.2. Homozygosity of R136S mutation protects against APOE4-induced p-Tau accumulation in human neurons.

a–d, Representative Western blot images (a) and quantification of APOE (b), PHF1-positive p-Tau (c), and AT8-positive p-Tau (d) levels in lysates of E4, E3, E4-S/S, or E4-R/S neurons. In b, APOE levels were normalized to those of E4. TUJ1 used as loading control [E4, n=32; E3, n=31; E4-S/S, n=64 (n=24 from E4-S/S-A; n=8 from E4-S/S-B; n=32 from E4-S/S-C); E4-R/S, n=59 (n=31 from E4-R/S-A; n=28 from E4-R/S-B)]. In c, PHF1-positive p-Tau levels were normalized to those of E4. TUJ1 used as loading control [E4, n=32; E3, n=31; E4-S/S, n=64 (n=24 from E4-S/S-A; n=8 from E4-S/S-B; n=32 from E4-S/S-C); E4-R/S, n=59 (n=31 from E4-R/S-A; n=28 from E4-R/S-B)]. In d, AT8-positive p-Tau levels were normalized to those of E4. TUJ1 used as loading control [E4, n=28; E3, n=27; E4-S/S, n=55 (n=16 from E4-S/S-A; n=11 from E4-S/S-B; n=28 from E4-S/S-C); E4-R/S, n=59 (n=31 from E4-R/S-A; n=28 from E4-R/S-B)]. **e**, Representative images showing immunostaining of p-Tau (PHF1), total Tau, and MAP2 in E4, E3, E4-S/S, or E4-R/S human neurons, with some PHF1+ puncta (white arrows). **f**, Quantification of fraction of the PHF1-positive area over MAP2-positive area (E4, n=25 fields of view; E3, n=25 fields of view; E4-S/S, n=38 fields of view; E4-R/S, n=33 fields of view). The ratio of PHF1 area over MAP2 area was normalized to that of E4. Western blot data were made up of at least 3 independent rounds of differentiation, and all data combined. Throughout, data are expressed as mean ± s.e.m. Differences between groups were determined by Welch's ANOVA followed with Dunnett T3 multiple comparison test; comparisons of P≤0.05 were labeled on graph.

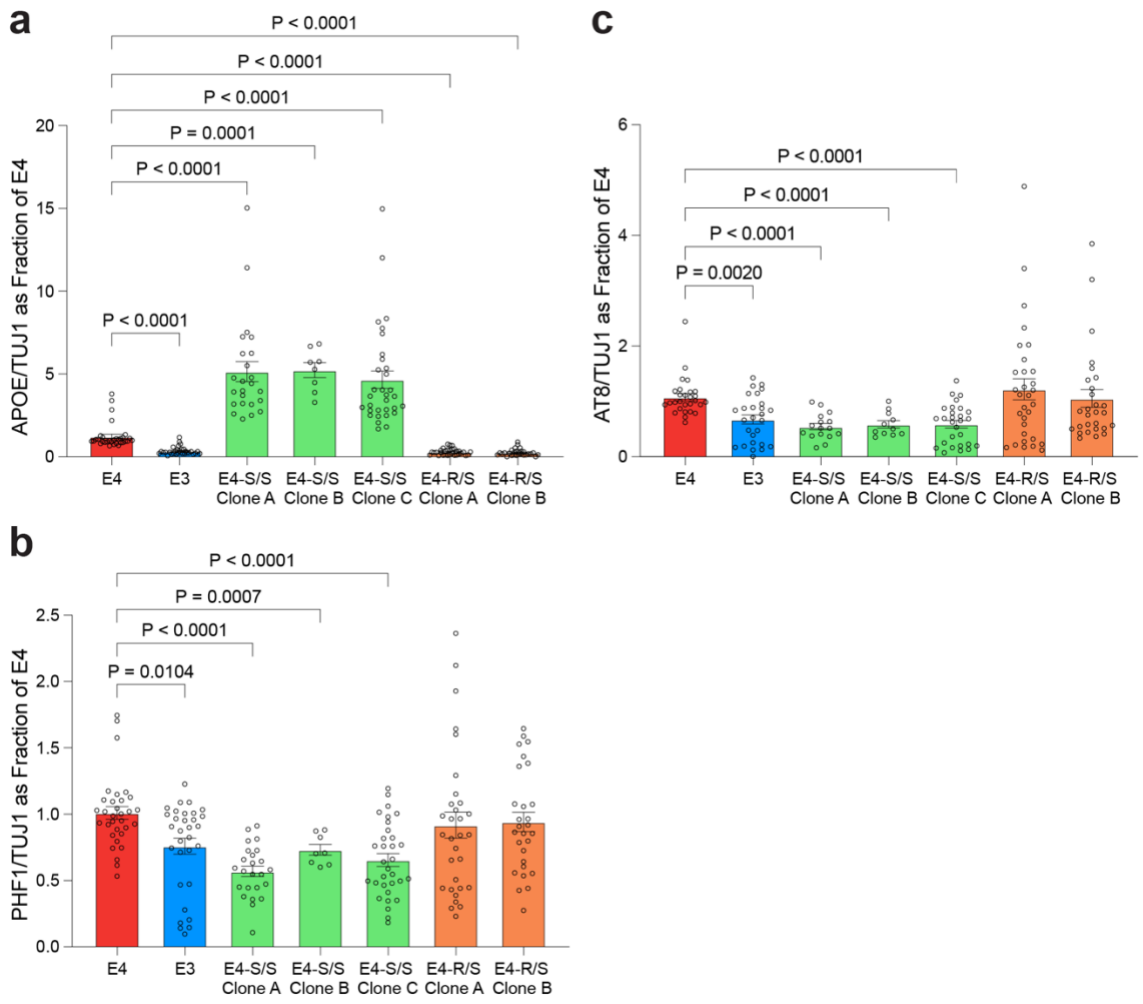

Figure 4.3. Levels of APOE and p-Tau in neuronal cultures derived from individual hiPSC lines with different APOE genotypes.

a, Quantification of APOE levels in neuronal lysates derived from individual hiPSC lines with different APOE genotypes. Values are normalized to E4. TUJ1 used as loading control (E4, n=32; E3, n=31; E4-S/S-A, n=24; E4-S/S-B, n=8; E4-S/S-C, n=32; E4-R/S-A, n=31; E4-R/S-B, n=28). **b**, Quantification of PHF1-positive p-Tau levels in neuronal lysates derived from individual hiPSC lines with different APOE genotypes. Values are normalized to E4. TUJ1 used as loading control (E4, n=32; E3, n=31; E4-S/S-A, n=24; E4-S/S-B, n=8; E4-S/S-C, n=32; E4-R/S-A, n=31; E4-R/S-B, n=28). **c**, Quantification of AT8-positive p-Tau levels in neuronal lysates derived from individual hiPSC lines with different APOE genotypes. Values are normalized to E4. TUJ1 used as loading control (E4, n=28; E3, n=27; E4-S/S-A, n=16; E4-S/S-B, n=11; E4-S/S-C, n=28; E4-R/S-A, n=31; E4-R/S-B, n=28). Western blot data were made up of at least 3 independent rounds of differentiation, and all data were combined. Throughout, data are expressed as mean ± s.e.m. Differences between groups were determined by Welch's ANOVA followed with Dunnett T3 multiple comparison test; comparisons of P≤0.05 were labeled on graph.

4.3 Homozygous R136S Mutation Reduces APOE4-Promoted Tau Uptake By Human Neurons Via HSPGs

Since the R136S mutation resulted in the reduction of APOE4-induced p-Tau accumulation in human neurons, we next investigated a potential underlying mechanism at play. We first tested if E4-S/S neurons exhibited an altered cellular distribution of p-Tau: on the cell surface versus intracellularly. We employed a low pH acid buffer wash (0.2M glycine/0.15M NaCl, pH 3.0) to broadly remove cell-surface-bound proteins. The low pH buffer disrupts the interactions between anionic proteoglycans of the plasma membrane and their ligands[70]. After treating neurons with the low pH buffer wash, we measured levels of p-Tau via Western blotting (**Fig. 4.5a,b**). Quantification of p-Tau in neuronal cultures after washing with the low pH buffer represents intracellular p-Tau levels. Likewise, quantification of p-Tau in neuronal cultures washed with a saline buffer represents total p-Tau levels (both intracellular and extracellular p-Tau). The amount of cell-surface-bound p-Tau was then inferred by the difference between total and intracellular p-Tau levels. E4-S/S neurons exhibited lower p-Tau levels both intracellularly and on the cell surface compared to E4 neurons (**Fig. 4.5b**). Furthermore, analysis of the proportion of cell-surface-bound versus intracellular p-Tau revealed that E4 neurons showed ~30% of p-Tau to be cell-surface-bound, while E4-S/S neurons displayed only ~10% of p-Tau as cell-surface bound (**Fig. 4.5c**). These data suggest that the APOE4-R136S mutation reduces the amount of p-Tau bound to the neuronal surface, potentially altering p-Tau uptake by neurons.

Recent findings show specifically that the anionic cell-surface receptors, HSPGs, mediate a large portion of neuronal uptake of Tau monomers and aggregates[50,93]. In cell culture systems, uptake of exogenous recombinant Tau can be competitively inhibited with the addition of heparin[50,93]. Notably, a major functional effect of the R136S mutation is a severely reduced binding affinity to heparin, as the point mutation occurs within the receptor-binding domain of APOE[41,43,44]. By contrast, APOE4 has increased binding affinity (up to two-fold) for heparin over APOE3[37–40].

We hypothesized that the reduction of APOE4-induced p-Tau accumulation by the R136S mutation was at least in part due to its defective HSPG binding and consequently the reduced Tau uptake promoted by APOE4 via cell surface HSPGs.

To test this hypothesis, we assessed the effect of the APOE4-R136S mutation on Tau uptake by human neurons. We first labeled recombinant Tau protein (2N4R) with Alexa-Fluor-488 fluorophore (Tau-488) and then treated neuronal cultures with 25nM Tau-488 (**Fig. 4.5d**), as reported previously[50,51,93]. Upon analysis via flow cytometry, we evaluated differences in the internalization of exogenous Tau-488 by human neurons with different APOE genotypes. Neurons were incubated for one hour at 37°C with either Tau-488 alone or Tau-488 together with 100μg/ml heparin to inhibit any Tau uptake via an HSPG-dependent pathway. We additionally repeated the experiments for all conditions at 4°C to prevent endocytosis so as not to conflate signal from surface-bound Tau-488 with internalized Tau-488. The detectable signal at 4°C was negligible at this concentration of Tau-488 and incubation time (**Fig. 4.4a**), as seen previously[50].

We analyzed the median fluorescence intensity (MFI), reflecting the median level of Tau-488 uptake at an individual cell level, in neurons with different APOE genotypes (**Fig. 4.5e**, **Fig. 4.4b,c**). The E4-S/S neurons exhibited a 50% reduction in MFI compared to E4 neurons (**Fig. 4.5e**), indicating reduced Tau-488 uptake by E4-S/S neurons. The E3 neurons also showed a trend of reduced Tau-488 uptake (~20%) compared to E4 neurons, although this is not significant. The E4-R/S neurons showed no significant difference in MFI versus E4 neurons (**Fig. 4.5e**), suggesting no alteration in Tau-488 uptake. The presence of heparin significantly reduced MFI in E4, E3, and E4-R/S neurons. However, the E4-S/S neurons trended towards a lower MFI, but this failed to reach significance (**Fig. 4.5e**). This indicated there was already decreased HSPG-dependent Tau uptake in these neurons. Importantly, E4 neurons treated with heparin exhibited reduced MFI (~40%) to levels not significantly different from E4-S/S neurons without heparin treatment. Furthermore, we quantified the percentage of Tau-488 positive cells, reflecting the proportion of cells with detectable levels of the internalized Tau-488 across the entire culture (**Fig.**

4.5f). Among E3, E4-S/S, and E4-R/S neuronal cultures, only E4-S/S neurons had a significantly reduced fraction (~30%) of cells with internalized Tau-488, as compared to E4 neurons (**Fig. 4.5f**). Heparin treatment reduced (~40%) the fraction of Tau-488 positive neurons in all groups, which aligns with previous studies showing Tau uptake via HSPG dependent pathways[50–52]. However, it is again notable that E4 neurons treated with heparin reduced the fraction of neurons with internalized Tau-488 to levels seen in E4-S/S neurons without heparin treatment. The effect of heparin treatment on the fraction of neurons with internalized Tau-488 was similar in E4 and E4-R/S neurons (**Fig. 4.5f**). Taken together, these data provide compelling evidence that E4-S/S, but not E4-R/S, neurons have reduced Tau uptake compared to E4 neurons, likely due to the defective HSPG binding of APOE4-R136S.

4.4 Homozygous R136S Mutation Protects Against APOE4-Induced p-Tau Accumulation in Part Due to Its Defective HSPG Binding

We next queried if the lowered HSPG-dependent Tau uptake seen in E4-S/S neurons was in fact contributing to protection against APOE4-induced p-Tau accumulation in human neurons. Thus, we designed an assay to test the relative long-term effect of heparin treatment on endogenous levels of p-Tau in neuronal cultures (**Fig. 4.5g**). hiPSC-derived neurons were treated with 100µg/ml heparin daily for three full days and then analyzed for p-Tau by Western blotting (**Fig. 4.5h**). Remarkably, this treatment lowered endogenous p-Tau levels in E4 neurons by ~25%, to a level more similar to that measured in untreated E4-S/S neurons (**Fig. 4.5i**). These data strongly support the notion that the defective HSPG binding of the R136S mutation contributes to the reduced APOE4-driven Tau pathology in human neurons.

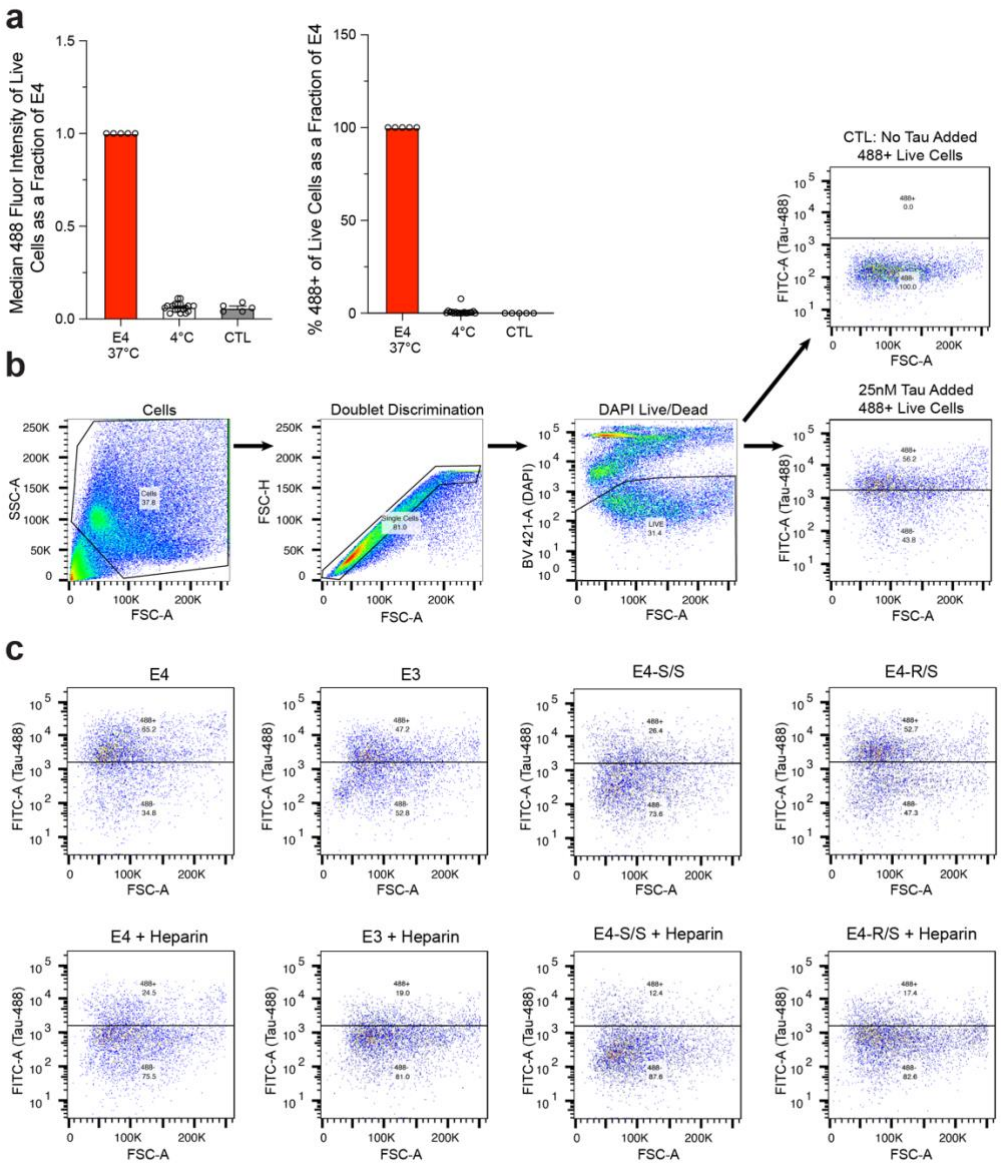

Figure 4.4. Measurement of neuronal uptake of Tau-488 by flow cytometry.
a, Internal controls of Tau-488 uptake assay as measured by median fluorescent intensity at 488nm of live cell population (left) or % 488-positive live cell population (right) via flow cytometry. All values normalized to E4 cells at 37°C, collected over five separate experiments. **b**, Gating strategy for Tau uptake assay. First, cells were gated on forward scatter/side scatter (FSC/SSC). Cells were then gated on forward scatter height (FSC-H) versus area (FSC-A) to discriminate doublets. Dead cells were removed from the analysis using nuclear stain with DAPI, and positive cells were determined by gating on a control (no Tau-488 added) population. **c**, Scatter plots of flow cytometry analysis of live cell population at 488nm (FITC-A versus FSC-A) for E4, E3, E4-S/S, or E4-R/S neuronal cultures with or without the treatment with 100µg/ml heparin. Roughly $1x10^5$ to $5x10^5$ events were counted in each experiment. The live cell population was down-sampled to 5000 cells for each sample.

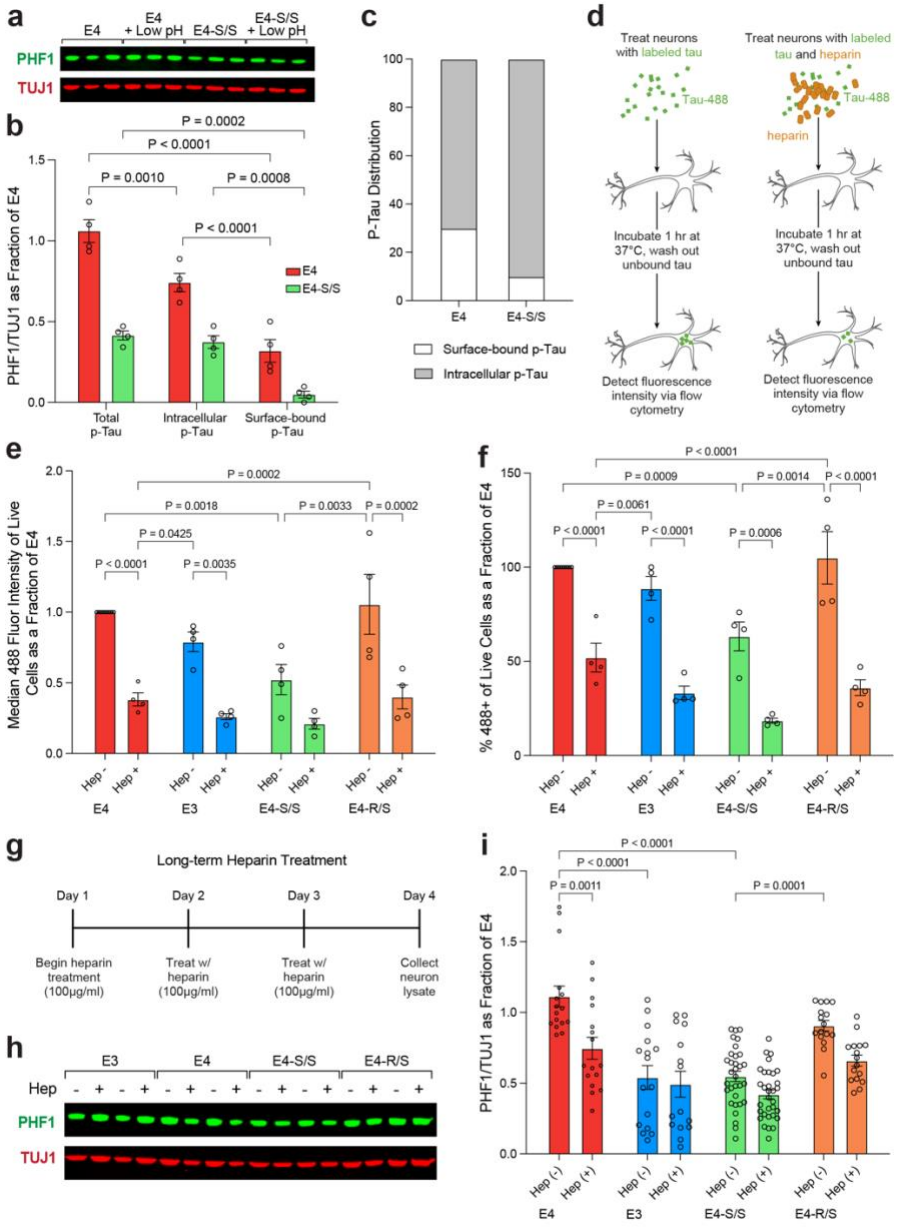

Figure 4.5. Homozygosity of R136S mutation protects against APOE4-induced p-Tau accumulation by reducing Tau update via the HSPG pathway.

a–c, Representative Western blot images (a) and quantification of PHF1-positive p-Tau levels (b) in lysates of E4 and E4-S/S neurons without or with low pH buffer wash. Values were normalized to those of E4. TUJ1 used as loading control (E4, n=4; E4+low pH, n=4; E4-S/S, n=4; E4-S/S +low pH, n=4). p-Tau distribution based on cellular localization (c). Of total PHF1-positive p-Tau levels detected per genotype, percentage of intracellular or surface-bound p-Tau were calculated. **d**, Diagram of Tau-488 uptake assay. Neurons treated with either Tau-488 alone (left) or Tau-488 together with 100µg/ml heparin (right) before flow cytometry analysis. **e**, Measurement of individual neuronal Tau-488 uptake (25nM, 1 hr) based on median fluorescence intensity per cell in E4 (n=9), E3 (n=4), E4-S/S (n=4), and E4-R/S (n=4) human neurons. **f**, Measurement of Tau-488 uptake (25nM, 1 hr) based on percent Tau-488 positive cells in E4 (n=9), E3 (n=4), E4-S/S

(n=4), E4-R/S (n=4) human neurons. All experiments in e,f were performed over four independent experiments and normalized to E4 median fluorescence intensity (e) or uptake (100%) (f). Analysis performed after Live cell population was down-sampled to 5000 cells for each sample. **g**, Experimental design for long-term heparin treatment of human neurons. **h, i**, Representative Western blot images (h) and quantification of PHF1-postiive p-Tau levels (i) in lysates of E4, E3, E4-S/S, or E4-R/S neurons under long-term heparin treatment. In i, PHF1-positive p-Tau levels were normalized to those of E4. TUJ1 used as loading control (E4, n=16; E4+heparin, n=16; E3, n=16; E3+heparin, n=15; E4-S/S, n=32; E4-S/S+heparin, n=32; E4-R/S, n=16; E4-R/S+heparin, n=16). Throughout, data are expressed as mean ± s.e.m. Differences between groups were determined by two-way ANOVA followed with Tukey's multiple comparison test; some comparisons of $P \leq 0.05$ were labeled on graph. Hep, heparin; fluor, fluorescence.

CHAPTER V: DISCUSSION AND CONCLUSIONS

The protection conferred by APOE3-R136S against early-onset AD caused by the PSEN1-E280A mutation is a milestone discovery[41]. It emphasizes the key roles of APOE variants in AD pathogenesis and/or protection. Our approach of studying APOE4-R136S allows us to investigate if and how this mutation may also be protective against AD pathologies promoted by APOE4 (**Fig. 5.1**). Our data show for the first time that homozygosity for the R136S mutation can fully protect against APOE4-driven Tau pathology, neurodegeneration, and neuroinflammation in a tauopathy mouse model (**Fig. 5.1**). We also demonstrate the protection of the APOE4-R136S mutation against Tau uptake and p-Tau accumulation in an AD-relevant context using human neurons (**Fig. 5.1**).

Prior work has shown that HSPGs are largely responsible for neuronal uptake of Tau[50–52,93]. Notably, by substituting a positively-charged arginine residue for the uncharged serine, the affinity of the receptor binding domain of APOE4-R136S for negatively charged HSPGs is greatly diminished[41,43,44]. We built upon these studies by generating isogenic hiPSC-derived neurons with APOE4 or APOE4-R136S to study the effect of R136S mutation on Tau uptake by human neurons. Our findings demonstrate that the R136S mutation reduces neuronal p-Tau accumulation at least partially by reducing APOE4-promoted Tau uptake due to the defective HSPG binding of APOE4-R136S. Thus, development of therapeutics targeting HSPG binding of APOE, especially APOE4, could be a viable approach to reduce Tau pathology and, consequently, its associated neurodegeneration and neuroinflammation.

Interestingly and importantly, the heterozygous R136S mutation partially protects against some of the detrimental effects of APOE4 (**Fig. 5.1**). Although PS19-E4-R/S mice and E4-R/S neurons did not show protection from APOE4-induced p-Tau accumulation, heterozygous R136S mutation is sufficient to fully rescue APOE4-promoted microgliosis and substantially reduces neurodegeneration. Heavier microgliosis correlates with hippocampal atrophy in PS19-E4 mice, but this relationship was completely abolished in PS19-E4-S/S mice and largely diminished in PS19-E4-R/S mice. The case of PS19-E4-R/S mice displaying high p-Tau burden yet fully

rescued microgliosis suggests that neurodegeneration-associated microgliosis is not solely induced by Tau pathology. This highlights the related but distinct roles of APOE variants in different AD pathologies, which likely depend on cell type. Furthermore, the R136S mutation has a gene dose-dependent effect on APOE4-promoted astrocytosis, with the homozygous mutation completely abolishing astrocytosis and the heterozygous mutation partially diminishing astrocytosis. Interestingly, a partial but substantial reduction in hippocampal atrophy was observed in PS19-E4-R/S mice. Greater astrocytosis correlates with hippocampal degeneration in PS19-E4 mice, a relationship that was eliminated in PS19-E4-S/S mice but maintained in PS19-E4-R/S mice. It is thus plausible to speculate that the remaining astrocytosis in PS19-E4-R/S mice, together with the Tau pathology, likely contributes to the remaining hippocampal atrophy.

We also examined the protective effects of APOE4-R136S mutation in a cell-type-specific manner by snRNA-seq analysis. Remarkably, there is a gene-dose-dependent effect of the R136S mutation on increasing disease-protective neuronal, astrocytic, and microglial subpopulations and decreasing disease-associated subpopulations of oligodendrocytes (DAOs), astrocytes (DAAs), and microglia (DAMs). The DAAs and DAMs have transcriptomic signatures similar to those reported previously in brains of AD patients and mouse models[87,88]. These disease-associated subpopulations were enriched in APOE4-expressing tauopathy mice and correlated to the severity of Tau pathology, neurodegeneration, and gliosis. Deeper analyses of DE genes revealed that these DAOs, DAAs, and DAMs each have unique transcriptomic signatures that are eliminated or even reversed with the homozygous APOE4-R136S mutation. These data indicate that the R136S mutation not only modifies APOE4-driven AD pathologies in general, but it also does so by differentially affecting the disease-associated transcriptomes in specific types of cells. Further analysis and validation of these cell type-specific effects in future studies may provide clues to the underlying cellular and molecular mechanisms of the AD protective R136S mutation of APOE.

Overall, this study illustrates the AD protective effects of the R136S mutation against APOE4-promoted pathologies in a gene-dose-dependent manner, both *in vivo* in a tauopathy mouse model and *in vitro* in hiPSC-derived neurons (**Fig. 5.1**). This study also provides potential molecular and cellular mechanisms by which the APOE-R136S mutation confers protection as potential targets for therapeutic development against APOE4-related AD and tauopathies.

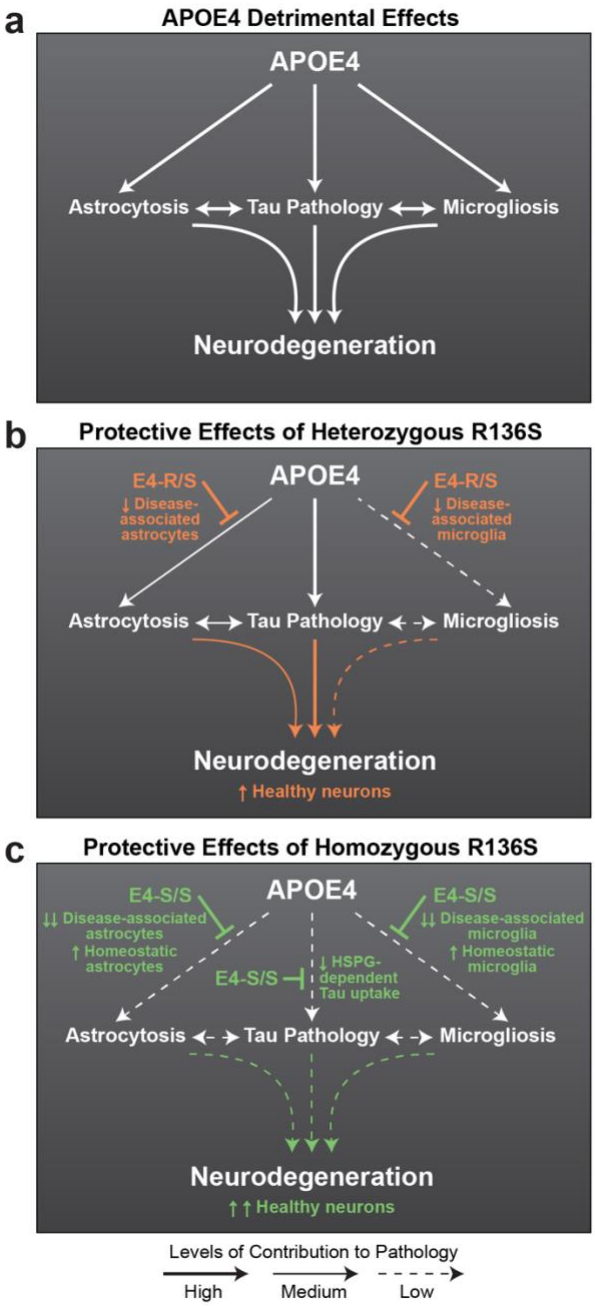

Figure 5.1. Diagram summarizing the dose-dependent protective effects of the R136S mutation on APOE4-driven AD pathologies.
a, APOE4 exacerbates AD pathologies, including Tau pathology, astrocytosis, microgliosis, and neurodegeneration. **b**, The heterozygous R136S mutation protects against APOE4-promoted gliosis by reducing disease-associated astrocytes and microglia, ultimately reducing neurodegeneration and increasing the population of healthy neurons. **c**, The homozygous R136S mutation protects against APOE4-promoted Tau pathology, in part due to reduced HSPG-dependent Tau uptake, and gliosis with further reduction of disease-associated astrocytes and microglia and increase in homeostatic astrocytes and microglia. This ultimately protects against neurodegeneration and leads to higher population of healthy neurons.

CHAPTER VI: FUTURE DIRECTIONS

While this study reveals key insights into both the mechanisms underlying APOE4-driven detrimental effects in AD and the protection of the R136S mutation against them, there are several potential research paths stemming from our initial studies.

Firstly, our snRNAseq findings indicate differential cell type specific protective effects of the R136S mutation. Further investigations of the mechanisms underlying these effects would be valuable to better understanding how to mitigate APOE4 toxicity, and ultimately provide pathways for therapeutic development.

Secondly, our study has some limitations. The original case report detailed strong protection of the APOE3-R136S mutation against autosomal dominant AD, particularly in the face of extremely high Aβ burden[41]. In the present study, we demonstrate the protective power of the R136S mutation against APOE4-driven effects in a tauopathy mouse model and in hiPSC-derived neurons from an AD patient, neither of which exhibit Aβ pathology. Thus, our study does not address the question as to whether the APOE-R136S mutation also protects against Aβ-mediated neuroinflammatory and neurodegenerative effects[94–98]. The field would benefit from such future studies. Furthermore, we strictly aimed to study if the R136S mutation overcomes the detrimental effects of APOE4, especially as a model for late-onset AD. The original patient showed AD protection with homozygous APOE3-R136S mutation[41]. It will be important for future studies to investigate whether the R136S mutation also provides protection against AD pathologies in the absence of APOE4.

Lastly, there are other rare APOE variants that confer protection against AD, including those in the lipid-binding region such as R251G. It would be a valuable addition to the field to better understand if and how these mutations may also overcome the detrimental effects of APOE4. Thus, future work could include the design and execution of a similar study to this one, only modeling another protective APOE variant.

REFERENCES

1. Hebert, L. E., Weuve, J., Scherr, P. A. & Evans, D. A. Alzheimer disease in the United States (2010-2050) estimated using the 2010 census. *Neurology* **80**, 1778–1783 (2013).
2. Huang, Y. & Mucke, L. Alzheimer Mechanisms and Therapeutic Strategies. *Cell* **148**, 1204–1222 (2012).
3. Mahley, R. W., Weisgraber, K. H. & Huang, Y. Apolipoprotein E4: A causative factor and therapeutic target in neuropathology, including Alzheimer's disease. *PNAS* **103**, 5644–5651 (2006).
4. Huang, Y. & Mahley, R. W. Apolipoprotein E: Structure and Function in Lipid Metabolism, Neurobiology, and Alzheimer's Diseases. *Neurobiol Dis* **72PA**, 3–12 (2014).
5. Holtzman, D. M., Herz, J. & Bu, G. Apolipoprotein E and Apolipoprotein E Receptors: Normal Biology and Roles in Alzheimer Disease. *Cold Spring Harb Perspect Med* **2**, (2012).
6. Koutsodendris, N., Nelson, M. R., Rao, A. & Huang, Y. Apolipoprotein E and Alzheimer's Disease: Findings, Hypotheses, and Potential Mechanisms. *Annu Rev Pathol* **17**, 73–99 (2022).
7. Harris, F. M., Brecht, W. J., Xu, Q., Mahley, R. W. & Huang, Y. Increased tau Phosphorylation in Apolipoprotein E4 Transgenic Mice Is Associated with Activation of Extracellular Signal-regulated Kinase: modulation by zinc. *J. Biol. Chem.* **279**, 44795–44801 (2004).
8. Wang, C. *et al.* Gain of toxic apolipoprotein E4 effects in human iPSC-derived neurons is ameliorated by a small-molecule structure corrector. *Nature Medicine* **24**, 647–657 (2018).
9. Shi, Y. *et al.* ApoE4 markedly exacerbates tau-mediated neurodegeneration in a mouse model of tauopathy. *Nature* **549**, 523–527 (2017).
10. Brecht, W. J. *et al.* Neuron-Specific Apolipoprotein E4 Proteolysis Is Associated with Increased Tau Phosphorylation in Brains of Transgenic Mice. *J. Neurosci.* **24**, 2527–2534 (2004).

11. Andrews-Zwilling, Y. *et al.* Apolipoprotein E4 Causes Age- and Tau-Dependent Impairment of GABAergic Interneurons, Leading to Learning and Memory Deficits in Mice. *J Neurosci* **30**, 13707–13717 (2010).
12. Li, G. *et al.* GABAergic Interneuron Dysfunction Impairs Hippocampal Neurogenesis in Adult Apolipoprotein E4 Knockin Mice. *Cell Stem Cell* **5**, 634–645 (2009).
13. Shi, Y. *et al.* Microglia drive APOE-dependent neurodegeneration in a tauopathy mouse model. *J Exp Med* **216**, 2546–2561 (2019).
14. Strittmatter, W. J. *et al.* Apolipoprotein E: high-avidity binding to beta-amyloid and increased frequency of type 4 allele in late-onset familial Alzheimer disease. *Proc. Natl. Acad. Sci. U.S.A.* **90**, 1977–1981 (1993).
15. Therriault, J. *et al.* APOEε4 potentiates the relationship between amyloid-β and tau pathologies. *Molecular Psychiatry* 1–12 (2020) doi:10.1038/s41380-020-0688-6.
16. Lin, Y.-T. *et al.* APOE4 Causes Widespread Molecular and Cellular Alterations Associated with Alzheimer's Disease Phenotypes in Human iPSC-Derived Brain Cell Types. *Neuron* **98**, 1294 (2018).
17. Zhao, J. *et al.* APOE4 exacerbates synapse loss and neurodegeneration in Alzheimer's disease patient iPSC-derived cerebral organoids. *Nat Commun* **11**, 5540 (2020).
18. Tesseur, I. *et al.* Expression of Human Apolipoprotein E4 in Neurons Causes Hyperphosphorylation of Protein Tau in the Brains of Transgenic Mice. *Am J Pathol* **156**, 951–964 (2000).
19. Braak, H. & Braak, E. Neuropathological stageing of Alzheimer-related changes. *Acta Neuropathol.* **82**, 239–259 (1991).
20. Theendakara, V., Bredesen, D. E. & Rao, R. V. Downregulation of protein phosphatase 2A by apolipoprotein E: Implications for Alzheimer's disease. *Molecular and Cellular Neuroscience* **83**, 83–91 (2017).

21. Mattsson, N. *et al.* Greater tau load and reduced cortical thickness in APOE ε4-negative Alzheimer's disease: a cohort study. *Alzheimer's Research & Therapy* **10**, 77 (2018).
22. Corder, E. H. *et al.* Gene dose of apolipoprotein E type 4 allele and the risk of Alzheimer's disease in late onset families. *Science* **261**, 921–923 (1993).
23. Farrer, L. A. *et al.* Effects of Age, Sex, and Ethnicity on the Association Between Apolipoprotein E Genotype and Alzheimer Disease: A Meta-analysis. *JAMA* **278**, 1349–1356 (1997).
24. Rebeck, G. W., Reiter, J. S., Strickland, D. K. & Hyman, B. T. Apolipoprotein E in sporadic Alzheimer's disease: Allelic variation and receptor interactions. *Neuron* **11**, 575–580 (1993).
25. Ward, A. *et al.* Prevalence of apolipoprotein E4 genotype and homozygotes (APOE e4/4) among patients diagnosed with Alzheimer's disease: a systematic review and meta-analysis. *Neuroepidemiology* **38**, 1–17 (2012).
26. Mahley, R. W. Apolipoprotein E: from cardiovascular disease to neurodegenerative disorders. *J Mol Med (Berl)* **94**, 739–746 (2016).
27. Zalocusky, K. A. *et al.* Neuronal ApoE upregulates MHC-I expression to drive selective neurodegeneration in Alzheimer's disease. *Nat Neurosci* **24**, 786–798 (2021).
28. Gale, S. C. *et al.* APOε4 is associated with enhanced in vivo innate immune responses in human subjects. *The Journal of allergy and clinical immunology* **134**, 127-134.e9 (2014).
29. Egensperger, R., Kösel, S., von Eitzen, U. & Graeber, M. B. Microglial activation in Alzheimer disease: Association with APOE genotype. *Brain Pathol* **8**, 439–447 (1998).
30. Overmyer, M. *et al.* Astrogliosis and the ApoE genotype. an immunohistochemical study of postmortem human brain tissue. *Dement Geriatr Cogn Disord* **10**, 252–257 (1999).
31. Minett, T. *et al.* Microglial immunophenotype in dementia with Alzheimer's pathology. *J Neuroinflammation* **13**, 135 (2016).

32. Xu, Q. *et al.* Profile and regulation of apolipoprotein E (ApoE) expression in the CNS in mice with targeting of green fluorescent protein gene to the ApoE locus. *J. Neurosci.* **26**, 4985–4994 (2006).

33. Xu, Q. *et al.* Intron-3 Retention/Splicing Controls Neuronal Expression of Apolipoprotein E in the CNS. *J Neurosci* **28**, 1452–1459 (2008).

34. Wetterau, J. R., Aggerbeck, L. P., Rall, S. C. & Weisgraber, K. H. Human apolipoprotein E3 in aqueous solution. I. Evidence for two structural domains. *J Biol Chem* **263**, 6240–6248 (1988).

35. Weisgraber, K. H. Apolipoprotein E: structure-function relationships. *Adv Protein Chem* **45**, 249–302 (1994).

36. Weisgraber, K. H., Rall, S. C. & Mahley, R. W. Human E apoprotein heterogeneity. Cysteine-arginine interchanges in the amino acid sequence of the apo-E isoforms. *J Biol Chem* **256**, 9077–9083 (1981).

37. Mahley, R. W. & Rall, S. C. Apolipoprotein E: Far More Than a Lipid Transport Protein. *Annual Review of Genomics and Human Genetics* **1**, 507–537 (2000).

38. Ji, Z.-S., Pitas, R. E. & Mahley, R. W. Differential Cellular Accumulation/Retention of Apolipoprotein E Mediated by Cell Surface Heparan Sulfate Proteoglycans. Apolipoproteins E3 and E2 greater than E4. *J. Biol. Chem.* **273**, 13452–13460 (1998).

39. Libeu, C. P. *et al.* New Insights into the Heparan Sulfate Proteoglycan-binding Activity of Apolipoprotein E. *J. Biol. Chem.* **276**, 39138–39144 (2001).

40. Yamauchi, Y. *et al.* Role of the N- and C-Terminal Domains in Binding of Apolipoprotein E Isoforms to Heparan Sulfate and Dermatan Sulfate: A Surface Plasmon Resonance Study. *Biochemistry* **47**, 6702–6710 (2008).

41. Arboleda-Velasquez, J. F. *et al.* Resistance to autosomal dominant Alzheimer's disease in an APOE3 Christchurch homozygote: a case report. *Nature Medicine* **25**, 1680–1683 (2019).

42. Liu, C.-C. *et al.* APOE3-Jacksonville (V236E) variant reduces self-aggregation and risk of dementia. *Science Translational Medicine* **13**, eabc9375 (2021).
43. Wardell, M. R., Brennan, S. O., Janus, E. D., Fraser, R. & Carrell, R. W. Apolipoprotein E2-Christchurch (136 Arg----Ser). New variant of human apolipoprotein E in a patient with type III hyperlipoproteinemia. https://www.jci.org/articles/view/113096/pdf (1987) doi:10.1172/JCI113096.
44. Lalazar, A. *et al.* Site-specific mutagenesis of human apolipoprotein E. Receptor binding activity of variants with single amino acid substitutions. *J. Biol. Chem.* **263**, 3542–3545 (1988).
45. Reiman, E. M. *et al.* Exceptionally low likelihood of Alzheimer's dementia in APOE2 homozygotes from a 5,000-person neuropathological study. *Nature Communications* **11**, 1–11 (2020).
46. Medway, C. W. *et al.* ApoE variant p.V236E is associated with markedly reduced risk of Alzheimer's disease. *Molecular Neurodegeneration* **9**, 11 (2014).
47. Le Guen, Y. *et al.* Association of Rare APOE Missense Variants V236E and R251G With Risk of Alzheimer Disease. *JAMA Neurology* (2022) doi:10.1001/jamaneurol.2022.1166.
48. Sepulveda-Falla, D. *et al.* Distinct tau neuropathology and cellular profiles of an APOE3 Christchurch homozygote protected against autosomal dominant Alzheimer's dementia. *Acta Neuropathol* (2022) doi:10.1007/s00401-022-02467-8.
49. Zalocusky, K. A., Nelson, M. R. & Huang, Y. An Alzheimer's-disease-protective APOE mutation. *Nature Medicine* **25**, 1648–1649 (2019).
50. Rauch, J. N. *et al.* Tau Internalization is Regulated by 6-O Sulfation on Heparan Sulfate Proteoglycans (HSPGs). *Sci Rep* **8**, 6382 (2018).
51. Stopschinski, B. E. *et al.* Specific glycosaminoglycan chain length and sulfation patterns are required for cell uptake of tau vs. α-synuclein and β-amyloid aggregates. *J. Biol. Chem.* jbc.RA117.000378 (2018) doi:10.1074/jbc.RA117.000378.

52. Holmes, B. B. & Diamond, M. I. Prion-like Properties of Tau Protein: The Importance of Extracellular Tau as a Therapeutic Target. *J. Biol. Chem.* **289**, 19855–19861 (2014).
53. Congdon, E. E. & Sigurdsson, E. M. Tau-targeting therapies for Alzheimer disease. *Nat Rev Neurol* (2018) doi:10.1038/s41582-018-0013-z.
54. Soeda, Y. & Takashima, A. New Insights Into Drug Discovery Targeting Tau Protein. *Frontiers in Molecular Neuroscience* **13**, (2020).
55. Yoshiyama, Y. *et al.* Synapse loss and microglial activation precede tangles in a P301S tauopathy mouse model. *Neuron* **53**, 337–351 (2007).
56. Bien-Ly, N., Gillespie, A. K., Walker, D., Yoon, S. Y. & Huang, Y. Reducing Human Apolipoprotein E Levels Attenuates Age-Dependent Aβ Accumulation in Mutant Human Amyloid Precursor Protein Transgenic Mice. *J. Neurosci.* **32**, 4803–4811 (2012).
57. Koutsodendris, N. *et al.* Neuronal APOE4 removal protects against tau-mediated gliosis, neurodegeneration and myelin deficits. *Nat Aging* 1–22 (2023) doi:10.1038/s43587-023-00368-3.
58. Liang, X., Potter, J., Kumar, S., Ravinder, N. & Chesnut, J. D. Enhanced CRISPR/Cas9-mediated precise genome editing by improved design and delivery of gRNA, Cas9 nuclease, and donor DNA. *Journal of Biotechnology* **241**, 136–146 (2017).
59. Stemmer, M., Thumberger, T., Keyer, M. del S., Wittbrodt, J. & Mateo, J. L. CCTop: An Intuitive, Flexible and Reliable CRISPR/Cas9 Target Prediction Tool. *PLOS ONE* **10**, e0124633 (2015).
60. Haeussler, M. *et al.* Evaluation of off-target and on-target scoring algorithms and integration into the guide RNA selection tool CRISPOR. *Genome Biology* **17**, 148 (2016).
61. Takahashi, K. & Yamanaka, S. Induction of pluripotent stem cells from mouse embryonic and adult fibroblast cultures by defined factors. *Cell* **126**, 663–676 (2006).
62. Takahashi, K. *et al.* Induction of pluripotent stem cells from adult human fibroblasts by defined factors. *Cell* **131**, 861–872 (2007).

63. Chen, Y.-H. & Pruett-Miller, S. M. Improving single-cell cloning workflow for gene editing in human pluripotent stem cells. *Stem Cell Research* **31**, 186–192 (2018).

64. Paquet, D. *et al.* Efficient introduction of specific homozygous and heterozygous mutations using CRISPR/Cas9. *Nature* **533**, 125–129 (2016).

65. Vakulskas, C. A. *et al.* A high-fidelity Cas9 mutant delivered as a ribonucleoprotein complex enables efficient gene editing in human hematopoietic stem and progenitor cells. *Nature Medicine* **24**, 1216 (2018).

66. Labun, K. *et al.* Accurate analysis of genuine CRISPR editing events with ampliCan. *Genome Res* **29**, 843–847 (2019).

67. Cradick, T. J., Qiu, P., Lee, C. M., Fine, E. J. & Bao, G. COSMID: A Web-based Tool for Identifying and Validating CRISPR/Cas Off-target Sites. *Mol Ther Nucleic Acids* **3**, e214 (2014).

68. Najm, R. *et al.* In Vivo Chimeric Alzheimer's Disease Modeling of Apolipoprotein E4 Toxicity in Human Neurons. *Cell Reports* **32**, 107962 (2020).

69. Schindelin, J. *et al.* Fiji: an open-source platform for biological-image analysis. *Nat Methods* **9**, 676–682 (2012).

70. Kameyama, S. *et al.* Acid wash in determining cellular uptake of Fab/cell-permeating peptide conjugates. *Peptide Science* **88**, 98–107 (2007).

71. Agarwala, R. *et al.* Database resources of the National Center for Biotechnology Information. *Nucleic Acids Res.* **44**, D7–D19 (2016).

72. Howe, K. L. *et al.* Ensembl 2021. *Nucleic Acids Res.* **49**, D884–D891 (2021).

73. Frankish, A. *et al.* GENCODE 2021. *Nucleic Acids Res.* **49**, D916–D923 (2021).

74. Zheng, G. X. Y. *et al.* Massively parallel digital transcriptional profiling of single cells. *Nat. Commun.* **8**, (2017).

75. Hao, Y. *et al.* Integrated analysis of multimodal single-cell data. *Cell* **184**, 3573-3587.e29 (2021).

76. Hafemeister, C. & Satija, R. Normalization and variance stabilization of single-cell RNA-seq data using regularized negative binomial regression. *Genome Biol.* **20**, 296 (2019).
77. Ahlmann-Eltze, C. & Huber, W. glmGamPoi: fitting Gamma-Poisson generalized linear models on single cell count data. *Bioinformatics* **36**, 5701–5702 (2021).
78. Wu, T. *et al.* clusterProfiler 4.0: A universal enrichment tool for interpreting omics data. *Innovation (N Y)* **2**, 100141 (2021).
79. Kanehisa, M., Sato, Y., Kawashima, M., Furumichi, M. & Tanabe, M. KEGG as a reference resource for gene and protein annotation. *Nucleic Acids Res.* **44**, D457–D462 (2016).
80. Benjamini, Y. & Hochberg, Y. Controlling the False Discovery Rate: A Practical and Powerful Approach to Multiple Testing. *J R Stat. Soc. Series B Stat. Methodol.* **57**, 289–300 (1995).
81. Bates, D., Mächler, M., Bolker, B. M. & Walker, S. C. Fitting Linear Mixed-Effects Models Using lme4. *J. Stat. Soft.* **67**, 1–48 (2015).
82. Shieh, G. & Jan, S.-L. Optimal sample size allocation for Welch's test in one-way heteroscedastic ANOVA. *Behav Res Methods* **47**, 374–383 (2015).
83. Jan, S.-L. & Shieh, G. Sample size determinations for Welch's test in one-way heteroscedastic ANOVA. *Br J Math Stat Psychol* **67**, 72–93 (2014).
84. Mahley, R. W. & Huang, Y. Apolipoprotein E Sets the Stage: Response to Injury Triggers Neuropathology. *Neuron* **76**, 871–885 (2012).
85. Blondel, V. D., Guillaume, J.-L., Lambiotte, R. & Lefebvre, E. Fast unfolding of communities in large networks. *J. Stat. Mech.* **2008**, P10008 (2008).
86. Kenigsbuch, M. *et al.* A shared disease-associated oligodendrocyte signature among multiple CNS pathologies. *Nat Neurosci* **25**, 876–886 (2022).
87. Habib, N. *et al.* Disease-associated astrocytes in Alzheimer's disease and aging. *Nat Neurosci* **23**, 701–706 (2020).

88. Keren-Shaul, H. *et al.* A Unique Microglia Type Associated with Restricting Development of Alzheimer's Disease. *Cell* **169**, 1276-1290.e17 (2017).

89. Ji, Z. S., Fazio, S., Lee, Y. L. & Mahley, R. W. Secretion-capture role for apolipoprotein E in remnant lipoprotein metabolism involving cell surface heparan sulfate proteoglycans. *J. Biol. Chem.* **269**, 2764–2772 (1994).

90. Mahley, R. W. & Huang, Y. Atherogenic remnant lipoproteins: role for proteoglycans in trapping, transferring, and internalizing. *J Clin Invest* **117**, 94–98 (2007).

91. Mahley, R. W., Weisgraber, K. H. & Huang, Y. Apolipoprotein E: structure determines function, from atherosclerosis to Alzheimer's disease to AIDS. *J. Lipid Res.* **50**, S183–S188 (2009).

92. Riddell, D. R. *et al.* Impact of Apolipoprotein E (ApoE) Polymorphism on Brain ApoE Levels. *J Neurosci* **28**, 11445–11453 (2008).

93. Holmes, B. B. *et al.* Heparan sulfate proteoglycans mediate internalization and propagation of specific proteopathic seeds. *PNAS* **110**, E3138–E3147 (2013).

94. Bloom, G. S. Amyloid-β and Tau: The Trigger and Bullet in Alzheimer Disease Pathogenesis. *JAMA Neurology* **71**, 505–508 (2014).

95. Hampel, H. *et al.* The Amyloid-β Pathway in Alzheimer's Disease. *Mol Psychiatry* **26**, 5481–5503 (2021).

96. Pereira, J. B. *et al.* Untangling the association of amyloid-β and tau with synaptic and axonal loss in Alzheimer's disease. *Brain* **144**, 310–324 (2021).

97. Geula, C. *et al.* Aging renders the brain vulnerable to amyloid beta-protein neurotoxicity. *Nat Med* **4**, 827–831 (1998).

98. Heneka, M. T. *et al.* Neuroinflammation in Alzheimer's disease. *Lancet Neurol* **14**, 388–405 (2015).

Publishing Agreement

It is the policy of the University to encourage open access and broad distribution of all theses, dissertations, and manuscripts. The Graduate Division will facilitate the distribution of UCSF theses, dissertations, and manuscripts to the UCSF Library for open access and distribution. UCSF will make such theses, dissertations, and manuscripts accessible to the public and will take reasonable steps to preserve these works in perpetuity.

I hereby grant the non-exclusive, perpetual right to The Regents of the University of California to reproduce, publicly display, distribute, preserve, and publish copies of my thesis, dissertation, or manuscript in any form or media, now existing or later derived, including access online for teaching, research, and public service purposes.

DocuSigned by:
Maxine Nelson
593A452BB96741D...
Author Signature

4/30/2023
Date